UNIVERSITY OF CALIFORNIA
RIVERSIDE

Approaches to Scalable, High Performance Electrodes for Next Generation Lithium-Ion Batteries

A Dissertation submitted in partial satisfaction
of the requirements for the degree of

Doctor of Philosophy

in

Materials Science and Engineering

by

Jingjing Liu

December 2018

Dissertation Committee:
Dr. Cengiz Ozkan, Co-Chairperson
Dr. Mihri Ozkan, Co-Chairperson
Dr. Kambiz Vafai
Dr. Roger Lake

The Dissertation of Jingjing Liu is approved:

_____

_____

_____

Committee Co-Chairperson

_____

Committee Co-Chairperson

University of California, Riverside

Acknowledgements

All the work presented in this dissertation could not have been done without the supports and encouragements from my supervisors, labmates, friends and family.

Firstly, I would like to express my sincerest appreciation to my advisor and co-advisor Dr. Cengiz S. Ozkan and Dr. Mihri Ozkan, respectively. They supported me with the upmost freedom to pursue projects I was interested. They also gave me lots of great advice to promote my projects. I would also like to thank my committee members, Dr. Kambiz Vafai and Dr. Roger Lake for serving as my committees in the dissertation defense.

I appreciate my labmates and friends: Changling Li, Chueh Liu, Zafer Mutlu, Yiran Yan, Kazi Ahmed, Rachel Ye and Jeffery Bell, Daisy Pation, Bo Dong, Yige Li. Without your generosity, suggestions and help, it would be hard to complete my Ph.D. degree.

Lastly, a heartful appreciation goes to my parents and my husband who supported me emotionally and financially. No words can express how grateful I am for all of your love. Thank you.

Copyright Acknowledgements

The text and figures in Chapter 2, in part or in full, are a reprint of the material as it appears in a completed work: Jingjing Liu, et al., “High Performance Si anodes for Lithium Ion Batteries with varying Magnesiothermic Reduction Conditions,” In Submission.

The text and figures in Chapter 3, in part or in full, are a reprint of the material as it appears in a completed work: Jingjing Liu, et al., “Scalable Coral-Like Si Powders with Three-Dimensionally-Interconnected Structures as Lithium Ion Battery Anodes,” In Submission.

The text and figures in Chapter 4, in part or in full, are a reprint of the material as it appears in the published work: Jingjing Liu, et al., “Facile and Scalable Synthesis of Copolymer-Sulfur Composites as Cathodes for High Performance Lithium-Sulfur Batteries,” MRS Advance, 2, 3271, 2017, (Reprinted with permission from RSC Publishing).

ABSTRACT OF THE DISSERTATION

Approaches to Scalable, High Performance Electrodes for Next Generation Lithium-Ion Batteries

by

Jingjing Liu

Doctor of Philosophy, Graduate Program in Materials Science and Engineering
University of California, Riverside, December 2018
Dr. Cengiz Ozkan, Co-Chairperson
Dr. Mihri Ozkan, Co-Chairperson

As the development of consumer devices and the application of electric vehicles, high energy-density lithium ion batteries (LIBs) are required. However, the energy density and capacity of current commercial LIBs are very limited because of the electrodes. Therefore, high energy-density and specific capacity electrodes materials are needed. Silicon is considered as the most promising next generation anode materials for LIBs due to their high energy density, high theoretical capacities (3600 mAh g^{-1}) and abundance. In this work, we synthesized coral-like Si powders with a three-dimensionally-interconnected structure via a facile and scalable maghesiothermic reduction method. The high porosity of the Si nanospheres can accommodate the volume expansion and release strain-stress within structure during lithiation and delithiation process, respectively. Besides, the coral-like and interconnected structure offers shorter

Li^+ diffusion path. The Si nanospheres based anode demonstrates a reversible capacity of 3172 mAh g^{-1} at high rate of C/2. After 500 cycles, the capacity retention is 1018 mAh/g, showing a fading rate 57%, with columbic efficiency more than 99%. We believe that, this low cost, facile and scalable synthesizing of porous Si nanospheres with interconnected network materials be widely used as Si based anodes for LIBs.

Since the capacity of lithium ion battery is decided by capacities of both electrodes, next-generation cathode materials also attract lots of interests. The sulfur-based cathode has attracted extensive attention because of its high capacity of 1672 mAh g^{-1} and its high abundance. However, the sulfur shuttling effects and the loss of active material during lithiation hinder its commercial application. To tackle these issues, we introduced polymerized organo-sulfur units to the elemental sulfur materials. The composite with 86% sulfur content was prepared using 1,3-diethynylbenzen and sulfur particles via scalable invers vulcanization. The sulfur content in copolymer sulfur was achieved as high as 86%. Our copolymer-sulfur composite cathode showed excellent cycling performance with a capacity of 454 mAh g^{-1} at 0.1 C after 300 cycles. We demonstrate that the organosulfur-DEB units in the sulfur cathode serve as the 'plasticizer' to effectively prevent the polysulfide shuttling.

Table of Contents

List of Figures

List of Tables

List of Abbreviations

SiNP	Silicon nanoparticle
CVD	Chemical vapor deposition
MTR	Magnesiothermic reduction
SEM	Scanning electron microscopy
TEM	Transmission electron microscopy
EDS/EDX	Energy dispersive x-ray sectroscopy
CE	Coulombic efficiency
CV	Cyclic voltammetry
PEIS	Potentiostatic electrochemical impedance spectroscopy
LIB	Lithium-ion battery
EV	Electric vehicle
SEI	Solid electrolyte interphase
EtOH	Ethanol
HF	Hydrofluoric acid
XRD	X-ray diffraction
BET	Brunauer-Emmet-Teller
TEOS	Tetraethyl orthosilicate
Nano-Si@C	Core-shell nano-silicon carbon
PAA	Poly(acrylic acid)

PVDF	Polyvinylidene fluoride
AB	Acetylene black
FEC	Fluoroethylene carbonate
EC	Ethylene carbonate
DMC	Dimethyl carbonate
NMP	N-methyl-2-pyrrolidone
DEB	1,3 diethynylbenzene
SS	Silica sphere
MPSS	Monodisperse Porous Silicon Sphere

Chapter 1 Instruction

1.1 History of Lithium Ion Batteries

The world is facing two main environmental issues: the shortage of fossil energy and carbon emissions. To lower the consumption of unrenewable fossil fuel, utilizing of renewable energy, such as biomass, solar energy, wind power, geothermal heat and hydroelectric energy, have been encouraged to be alternative. Additionally, carbon emission is increased continuously in the past 150 years because of human being's activities [1]. As shown in Fig. 1.1, there are about 28% of the carbon emission is associated to the transportation, which is caused by the burning of gasoline in the combustion engine.

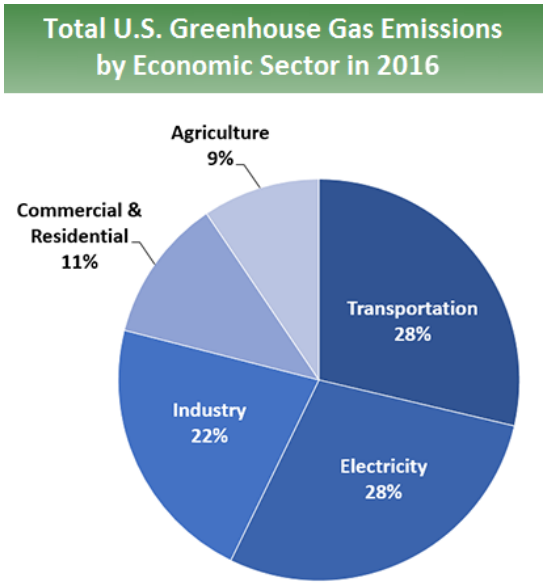

Fig.1. 1 Carbon Emission by Sectors in 2016 (Figure adopted form EPA)

Accordingly, the wide use of electric vehicles (EVs) can effectively mitigate the greenhouse gas release and decrease the consumption of fossil fuel. There are several different types of batteries which can be used in EVs: flooded lead-acid batteries [2], nickel-metal hydride batteries [3], sodium batteries [4] and LIBs [5]. LIBs have attracted most attentions, due to its high energy-density, low operation voltage, relative low rate of self-discharge and low maintenance needed [6]. G.N lewis began to work on the lithium batteries in 1912, but it was not commercialized until early 1970s[7,8]. These attempts using lithium metals as anodes failed due to its safety problems caused by inherent instability of lithium metals during charging and discharging. The growing dendrites on the surface of lithium metals would cause the shortcuts of batteries, leading to fire or explosion further. A strong research effort was mounted to convert lithium-metal batteris to non-metallic lithium batteries using lithium ions. Yazami[9] achieved the first secondary, or rechargeable, Li-ion battery in 1983, based on the intercalation graphite anode proposed by Besenhard[7] and Eichinger[8] in 1976. In 1991, Sony corporation produced first commercially available LIB with graphite anode and $LiCoO_2$ (LCO) cathode, developed by Goodenough in 1980[10]. Nowadays, the commercial LIBs are comprised by a lithium metal oxide cathode ($LiCoO_2$, NCA, etc.) and a graphite anode. Graphite is widely used as anode material for LIBs because of its excellent stability over thousands of cycles, good conductivity and relatively low price compared to other anode materials [11,12]. Since the advent of first commercial LIBs, the electrode materials have been unchanged for

more than 20 years, due to their low cost, high stability over thousands of cycles, and relative fast charging time.

The trend of increasing battery energy density respect to time since 1991 is illustrated in Fig. 1.2. The energy density of commercial LIBs was increased over time in every 10 years. Nonetheless, the incremental pace of performance is not sufficient for need of consumer electron devices, and EVs. To meet the demand for consumer electron devices and EVs, a leap in energy density, which can make LIBs comparable to gasoline combustions, is necessary.

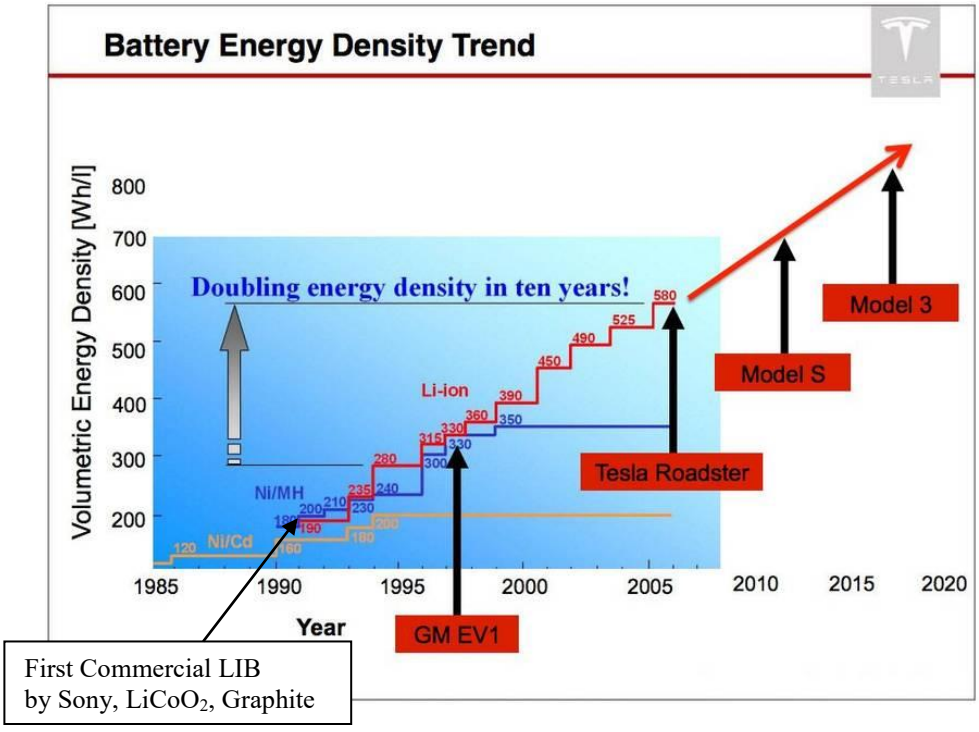

Fig.1. 2 Trend of Battery Energy Densities Over Years (Figure Adopted from Tesla)

1.2 Silicon as a Next-Generation Anode for LIBs

To achieve the high energy-density batteries for EVs, consumer electronics, and lower usage of petroleum, scientists are seeking new electrode materials with higher theoretical capacities and energy densities. Lots of materials have been studied as the alternative for graphite anodes, germanium[13], tin[14], 2D-carbon[15], TiO_2 [16], and silicon[17] and so on. Various proposed anode materials are displayed with their theoretical specific capacities (electric charge per unit mass) in Fig. 1.3[18]. All the discharge potentials are measured versus Li metal, which means the lower reductive potential highly possibly leads to higher charge-discharge voltage range of full cells. While the potential of full cells is the difference between the cathode lithiation potential and the anode delithiation potential, the higher difference means greater energy density, based on the equation of $E = 0.5*C*V^2$ (E:Energy density, Wh kg^{-1}; C: Capacity, Ah g^{-1}; V: full cell voltage, V)[19]. From Fig. 1.3[20], we can find that silicon has the highest theoretical specific capacity of 4200 mAh^{-1}, but it can be only achieved at temperature higher than melting point of Li. At room temperature, the theoretical specific capacity of silicon is calculated to be 3579 mAh g^{-1}, from a $Li_{15}Si_4$ phase. Although Li metal is the most ideal anode material, due to its high conductivity, lightest weight, highest theoretical specific capacity (3860 $mAhg^{-1}$), there is inherently instable formation of lithium dendrites on the surface of lithium anode, which will cause shortcut, even explosion of batteries. Besides, lithium metal is very sensitive to moisture and oxygen, thus, all experiments related to lithium metals must be operated in inert environment, which will be very costly. Recently, people are working on

solid state electrolytes to buffer the inherent deformation of lithium dendrites on the surface of lithium anode to overcome the challenges mentioned above. However, it is still a lot of work to do to commercialize the lithium metals.

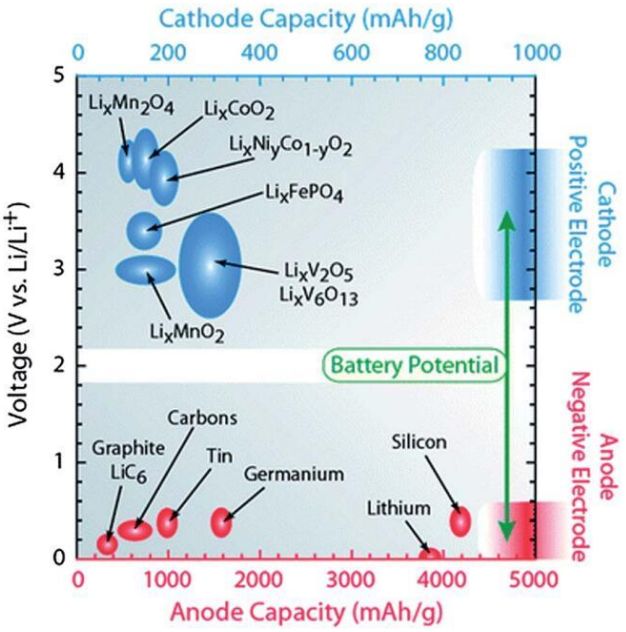

Fig.1. 3 Illustration of Cathode and Anode Materials According to Their Theoretical Specific Capacities and Reduction Potentials[20]

Hence, the next generation anode materials listed in Fig. 1.3 have attracted lots attentions, especially silicon. Silicon has been considered as one of the most promising anode material in decades due to its high abundance (as shown in Fig. 1.4), highest theoretical capacity of 3579 mAh g^{-1} besides lithium metal, and non-toxic property.

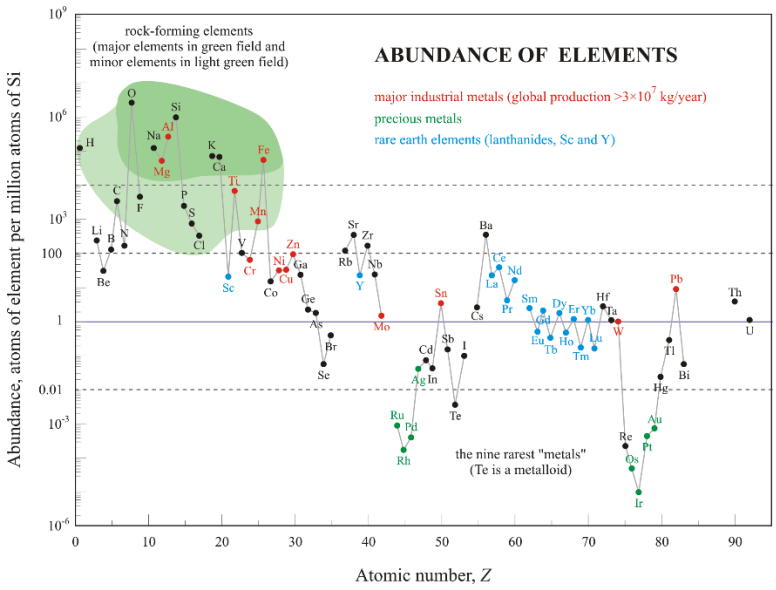

Fig.1. 4 Relative Abundance of Elements in Earth Versus Atomic Numbers (Figure from U.S. Geological Surver, 2005)

However, there are obstacles to prevent the commercialization of silicon anodes: extremely large volume expansion during lithiation and delithiation, low conductivity and degradation of the SEI layer during cycling[17]. The large volume expansion is caused by the alloy process to form metastable $Li_{3.75}Si$ when batteries are charging. After several charging/discharging cycles, the volume expansion introduces large stress during lithiation, which leads to the mechanical failure, even the pulverization of silicon anodes, as shown in Fig.1.5 (a)[17]. Pulverization of silicon anodes may let silicon materials separate from the current collects and conductor additives (Acetylene Black), which

further loses electrical conductivities of whole batteries (shown in Fig. 1.5 (b)). Moreover, the expansion consumes extra electrolytes and cause the degradation of the SEI layer. Because when the silicon anode is delithiated, the SEI layer can't go back to its original form, cracks and repeatedly exposes rare silicon surface to electrolytes to form SEI (as shown in Fig. 1.5 (c))[17]. The inherent formation of SEI lays consumes Li ions and electrolytes, which also decrease the columbic efficiency[17]. Besides, the thicker SEI layers increase the impedances of batteries.

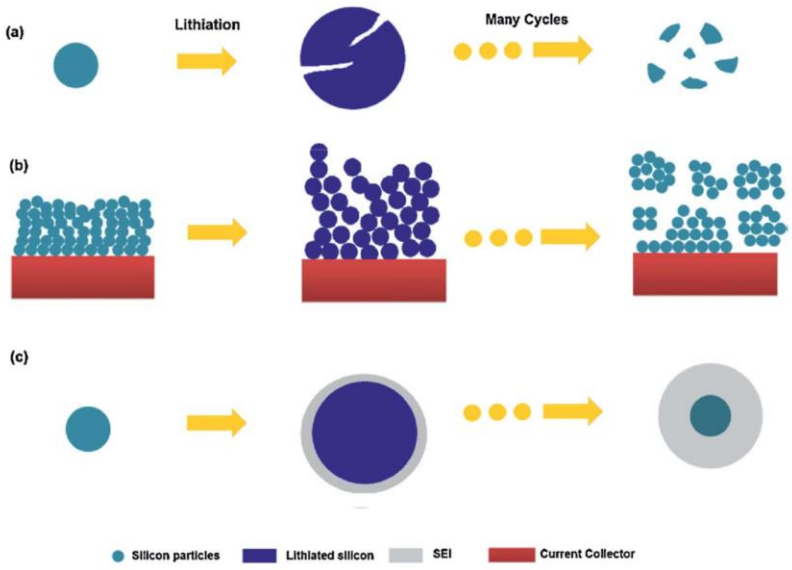

Fig.1. 5 SEI Fracture and Growth during cycles[17]

To mitigate the volume expansion, nanostructured silicon anodes have been studied[21-27], which shows improved electrochemical cycling performance. In these nanosized structures, there are fair spaces to accommodate the volume expansion and

strain introduced during lithiation. Additionally, Liu et.al[28] indicated the critical diameter of nanosized silicon materials, beyond which the silicon anodes would crack or pulverize.

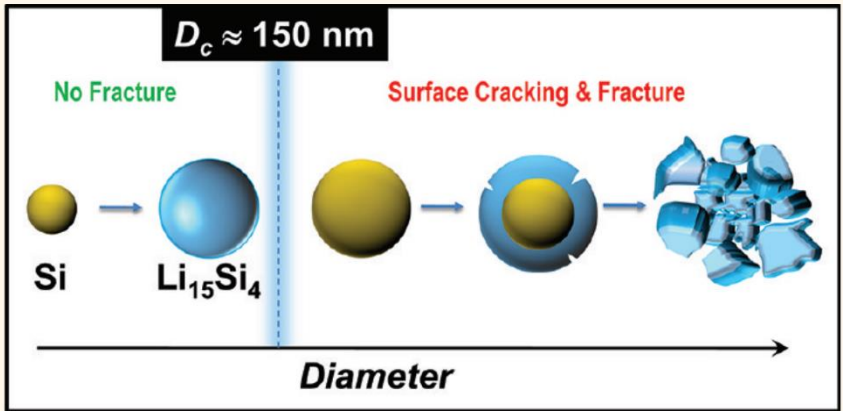

Fig.1. 6 Illustration to Size Dependence of Fracture[28]

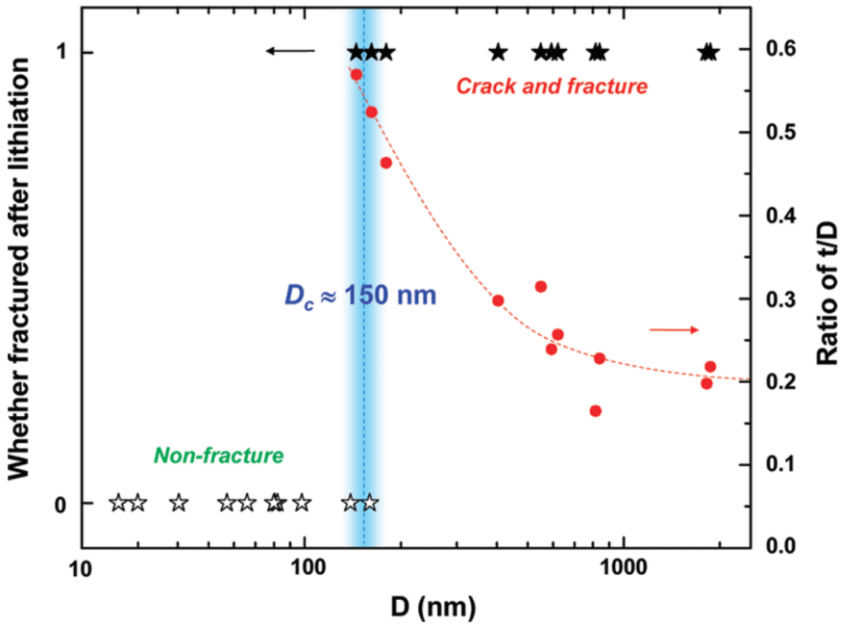

Fig.1. 7 Statistics showing the critical size (Dc) around 150nm[28]

Liu et al.[28] demonstrated that silicon nanoparticles could be fully lithiated to Li-Si alloy of $Li_{15}S_4$ without cracking when the diameter was less than a critical size of 150 nm. The unexpected fracture was associated to the development of tension in the surface layers, caused by a lithiation mechanism in crystalline silicon anodes. Accordingly, we tried several techniques to synthesize nanosized silicon nanoparticles as the next-generation anode materials for LIBs.

1.3 Sulfur as new cathode materials for LIBs

The total capacity of a lithium ion battery is limited by capacities of both anode and cathode, as shown below[29]:

$$\frac{1}{C_{cell}} = \frac{1}{C_{anode}} + \frac{1}{C_{cathode}}$$

We already discussed the future application of silicon anodes above, however, the commercial insertion cathode materials, such as $LiCoO_2$ (272 $mAhg^{-1}$), and $LiFePO_4$ (170mAh g^{-1}), have limited capacities which can't meet the demand for EVs and consumer electron devices. Hence, studies on next-generation, high-capacity cathode materials, such as sulfur[30,31] (1675 mAh^{-1}), Li_2S[32,33] (1166 $mAhg^{-1}$) and oxygen[34] (3842 $mAhg^{-1}$ in a lithium-air battery) have been done a lot recently. Sulfur is proposed as one of the promising cathode materials due to its high abundant, highest theoretical specific capacity, and environmentally friendly. However, there are several issues impeding application of sulfur cathodes. During lithiation process, sulfur undergoes multiple steps[35]:

$$S_8 + 2e^- \rightarrow S_8^{2-}$$

$$3S_8^{2-} + 2e^- \rightarrow 4S_6^{2-}$$

$$2S_6^{2-} + 2e^- \rightarrow 3S_4^{2-}$$

$$S_4^{2-} + 4Li^+ + 2e^- \rightarrow 2Li_2S_2$$

$$Li_2S_2 + 2Li^+ + 2e^- \rightarrow 2Li_2S$$

The first 3 steps occur at high voltage plateau (2.15 V-2.4 V), and the products, S_8^{2-}, S_6^{2-} and S_4^{2-}, are soluble in the electrolytes. These soluble long-chain polysulfides are dissolved in electrolytes and transfer to the surface of anodes. When sulfur cathodes are further discharged to low voltage at 2.1 V, long-chain soluble polysulfides are lithiated to short-chain insoluble lithium-sulfides, Li_2S, at the surface of anodes and sulfur cathodes[35]. The soluble polysulfide transfer between anode and cathode, causing loss of active materials and poor cycle life and low columbic efficiency. This phenomenon is named as 'shuttling effect' for sulfur cathode shown in Fig. 1.8[36]. In addition, the conductivity of Li_2S is very low, when the Li_2S deposited on the surface of sulfur cathodes and anodes, it will impede the transferring of Li^+, electrons and further lithiation of anodes, delithiation of cathodes. Many strategies have been done to solve polysulfide shuttling, such as mechanical barriers/trapping, chemical suppression, conductive network and electrolyte additives[35].

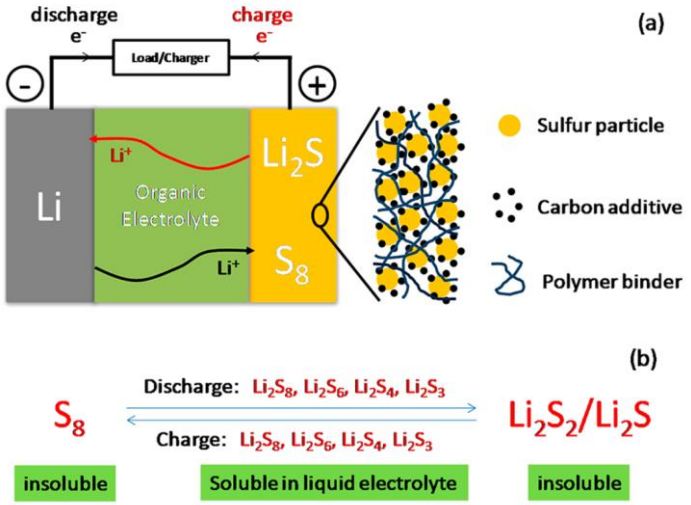

Fig.1. (a)Illustration of Charging/Discharge process of Li-S Cells. (b) Formation of Soluble and Insoluble Polysulfide

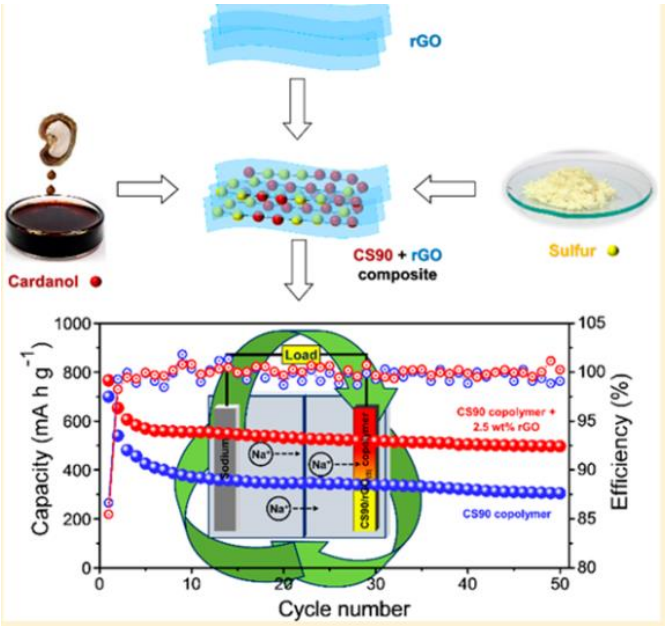

Fig.1. 8 Illustration of Graphene-Sulfur Copolymer Materials[37]

Among all the strategies, the novel carbon and sulfur compounds with functional carbon groups is the most attractive. The functional carbon group is available to adsorb sulfur or soluble polysulfides during lithiation, which can block the 'shuttling'. This chemical adsorption, such as graphene-sulfur copolymer shown in Fig.1.9[37], shows an excellent cycling stability due to the high utilization of active sulfur materials, which is much better than the traditional sulfur-carbon composites based on physical barrier to prevent dissolution of polysulfide. This route is attractive and encouraging, but there are limited carbon materials with functional groups, which can be chemically bonded to sulfur or polysulfide. Moreover, special chemical structures are required to achieve these strong interactions. Herein, we propose a new chemical processor to realize the chemically strong bonding to stabilize the sulfur cathodes.

1.4 Novel Full Cell Configuration for Silicon-Sulfur Batteries

Hall-cell configuration is often used to study the properties of active materials by eliminating the other possible variables. The half-cell configuration comprises a lithium-metal counter electrode, and a studied active-material based electrode. Most researches related to silicon anodes and sulfur cathodes are characterized in half-cell configuration.

In consideration of above discussion, silicon and sulfur are the most promising electrode materials for LIBs, thus, the full cells comprising sulfur cathodes and silicon anodes are attractive. They have a high theoretical energy density of 1982 Wh/kg, which is three times of the currently commercial LIBs'. However, the only lithium source in the

electrolyte is not enough for the whole cell, the either lithiated electrode is required here. While lithium sulfide is hazardous and, both lithium sulfide and lithium silicide are sensitive and costly to operate them[38-40]. Hence, Ye et.al[41] in our group proposed a facile alternative to prelithiated sulfur-silicon full cell systems, shown in Fig. 1.10. The lithium chip sitting at the top of silicon anodes acts as a lithium source for the whole battery. The direct contact between lithium chip and Cu current collector make it possible for electrons to transfer to the cathode. This novel sulfur-silicon-full-cell demonstrates a high energy density of 350 Wh/kg over 250 cycles at a rate of C/10, and this novel method will pave a way for further study on sulfur and silicon full cells in the future.

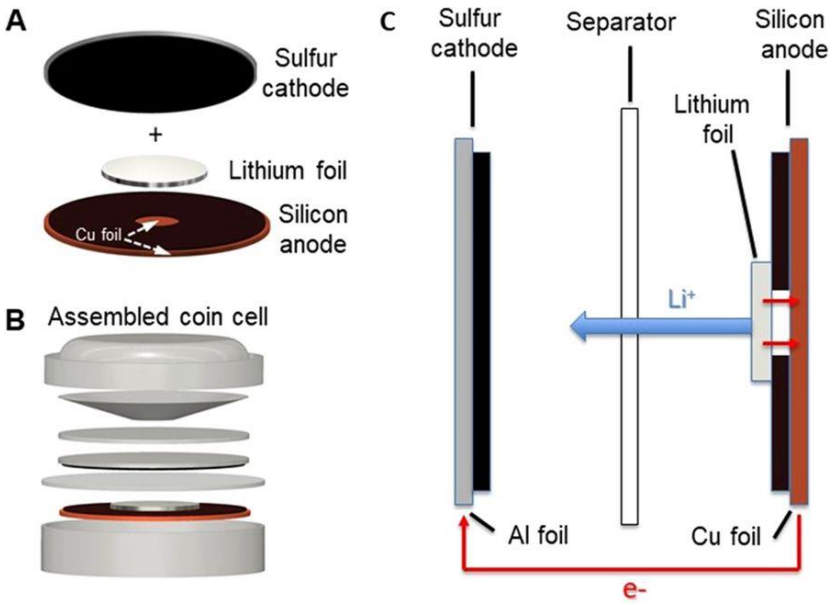

Fig.1. 9 Schematic of Silicon-Sulfur Batteries

1.5 Reference

1. Solomon, S., D. Qin, M. Manning, Z. Chen, M. Marquis, K.B. Averyt, M. Tignor and H.L. Miller, Cambridge University Press, Cambridge, United Kingdom and New York, NY, USA.IPCC (2007).

2. Barre, Harold,. Summer Breeze Publishing. pp. 63–65. ISBN 0-9647386-1-9 (1997).

3. K. Hasegawa, International journal of research in physical chemistry and chemical physics (1994).

4. Y. Lu, L. Wang, J. Cheng and J. B. Goodenough, Chem. Commun. 48, 6544-6546 (2012)

5. C. Li, C. Liu, W. Wang, J. Bell, Z. Mutlu, K. Ahmed, R. Ye, M. Ozkan and C. S. Ozkan, Chem. Commun., 52, 11398, (2016).

6. L. Hu, H. Wu, S. S. Hong, L. Cui, J. R. McDonough, S. Bohy and Y. Cui, Chem. Commun., 47, 367, (2011)

7. L. Hu, H. Wu, S. S. Hong, L. Cui, J. R. McDonough, S. Bohy and Y. Cui, Chem. Commun., 47, 367, (2011).

8. Eichinger, G. & Besenhard, J. O. J. Electroanal. Chem. Interfacial Electrochem. 72, 1-31 (1976).

9. Yazami, R. & Touzain, P. J. Power Sources 9, 365-371 (1983).

10. Mizushima, K., Jones, P. C., Wiseman, P. J. & Goodenough, J. B. Mater. Res. Bull. 15, 783-789 (1980)

11. Fukuda, K., Kikuya, K., Isono, K. & Yoshio, M. J. Power Sources 69, 165-168 (1997).

12. Lu, M., Cheng, H. & Yang, Y. Electrochim. Acta 53, 3539-3546 (2008).

13. M. Park, K. Kim, J. Kim and J. Cho, Adv. Mater. 22, 415 (2010).

14. W. Zhang, J. Hu, Y. Guo, S. Zheng, L. Zhong, W. Song, L. Wan, Adv. Mater. 20, 1160 (2008).

15. H. Wang, Z. Wu, F. Meng, D. Ma, X. Huang, L. Wang, X. Zhang, ChemSusChem, 6, 56 (2012).

16. B. He, B. Dong, H. Li, Electrochem. Comm. 9, 425 (2007).

17. H. Wu, Y. Cui, Nanotoday, 7, 414 (2012).

18. M. Osiak,a H. Geaney,ab E. Armstronga and C. O'Dwye, J. Mater. Chem. A, 2,9344 (2014).

19. C. Li, C. Liu, W. Wang, Z. Mutlu, J. Bell, K. Ahmed, R. Ye, M. Ozkan and C. S. Ozkan, Sci. Rep., 7, 917, (2017)

20. M. Osiak, H. Geaney, E. Armstronga and C. O'Dwyer, J. Mater. Chem. A, 2, 9433 (2014).

21. Magasinski, A.; Dixon, P.; Hertzberg, B.; Kvit, A.; Ayala, J.; Yushin, G. Nat. Mater., 9, 461 (2010).

22. Chan, C. K.; Peng, H. L.; Liu, G.; McIlwrath, K.; Zhang, X. F.; Huggins, R. A.; Cui, Y. Nat. Nanotechnol., 3, 31 (2008).

23. Takamura, T.; Ohara, S.; Uehara, M.; Suzuki, J.; Sekine, K. J. Power Sources, 129, 96 (2004).

24. Cui, L. F.; Ruffo, R.; Chan, C. K.; Peng, H. L.; Cui, Y. Nano Lett. 9, 491 (2009).

25. Park, M. H.; Kim, M. G.; Joo, J.; Kim, K.; Kim, J.; Ahn, S.; Cui, Y.; Cho, J. Nano Lett. 9, 3844 (2009).

26. Zhao, K.; Wang, W. L.; Gregoire, J.; Pharr, M.; Suo, Z.; Vlassak, J.; Kaxiras, E. Nano Lett. 11, 2962 (2011).

27. Zhao, K. J.; Pharr, M.; Vlassak, J. J.; Suo, Z. G. J. Appl. Phys. 109, 016110 (2011).

28. X. Liu, L. Zhong, S. Huang, S. X. Mao, T. Zhu, and J. Huang, ACS Nano, 6, 1522 (2012).

29. K. Eom, T. Joshi, A. Bordes, I. Do and T. F. Fuller, J. Power Sources, 249, 118, (2014)

30. Ji, L.; Rao, M.; Zheng, H.; Zhang, L.; Li, Y.; Duan, W.; Guo, J.; Cairns, E. J.; Zhang, Y. J. Am. Chem. Soc.,133, 18522 (2011).

31. Ji, L. W.; Rao, M. M.; Aloni, S.; Wang, L.; Cairns, E. J.; Zhang, Y. G. Energy Environ. Sci. 2011, 4, 5053 (2011).

32. Y. Chen and P. Kaghazchi, Nanoscale, 6, 13391 (2014).

33. A. Hayashi, R. Komiya, M. Tatsumisago, T. Minami, Solid State Ionics, 152, 285 (2002).

34. G. Girishkumar, B. McCloskey, A. C. Luntz, S. Swanson, and W. Wilcke, J. Phys. Chem. Lett.,1, 2193 (2010).

35. Y. Yang, G. Zheng and Y. Cui, Chem. Soc. Rev., 42, 3018 (2013).

36. A. Manthiram, Y. Fu, S.-H. Chung, C. Zu and Y.-S. Su, Chem. Rev., 114, 11751 (2014).

37. A. Ghosh, S. Shukla, M. Monisha, A. Kumar, B. Lochab,and S. Mitra, ACS Ener. Lett., 2, 2478, (2017).

38. Y. Yang, M. T. McDowell, A. Jackson, J. J. Cha, S. S. Hong and Y. Cui, Nano letters10.4 (2010): 1486-1491.

39. J. Hassouna, J. Kimb, D. Lee, H. Jung, S. Lee, Y. Sun, B. Scrosati, Journal of Power Sources ,202 (2012): 308-313.12

40. N. Liu, L. Hu, M. T. McDowell, A. Jackson, and Y. Cui, ACS nano 5.8 (2011): 6487-6493

41. R. Ye, J. Bell, D. Patino, K. Ahmed, M. Ozkan and C. S. Ozkan, Scientific Rep., 7, 17264 (2017).

Chapter 2 Monodisperse Silicon Nanoparticles via Magnesiothermic Reduction with Varying Reduction Parameters

2.1 Silicon Synthesis Routes

The main synthesis route for silicon production in industry is carbothermic reduction. In the routes illustrated in Fig. 2.1, the pure silica achieved from precursor, diatom, beach sand, rice husks and so on, is mixed with reducing carbon agent (eg. graphite, charcoal), and heated to 2000ºC[1,2] in an electric arc furnace for industrial scale. The reaction is shown as bellow:

$$SiO_2\ (s) + 2C\ (s)\ \rightarrow\ Si(s) + 2CO\ (g)$$

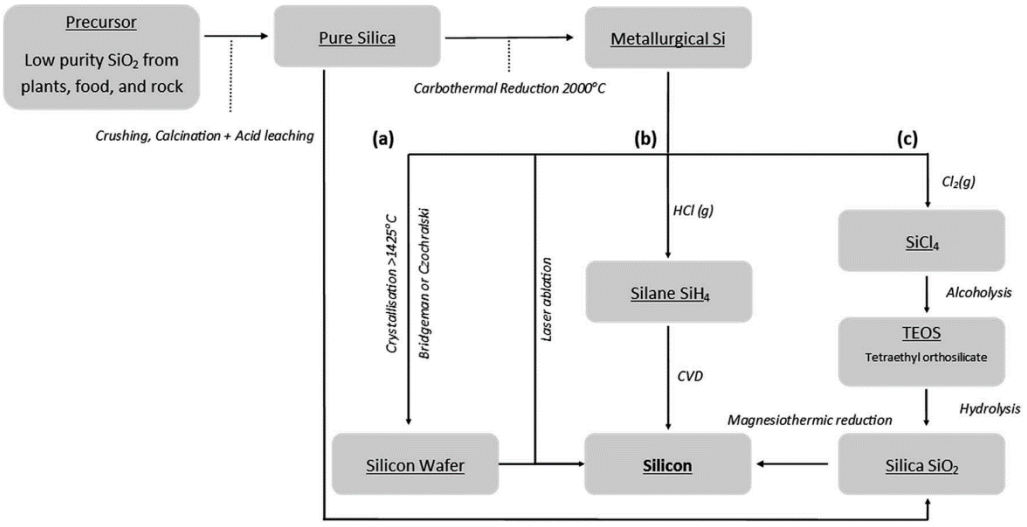

Fig.2. 1 Chart of Silicon Synthesis Routes

Apparently, the byproducts of carbothermic reduction is CO (g), which is easily oxidized to CO_2 in air, to increase the emission of greenhouse gas[3]. A further refinement of these produced silicon relies on crystallization of molten silicon, which requires high temperature (> 1414 ºC). Though this method can yield large scale of silicon, it consumes large amount of energy and emit several tons of greenhouse gas per year, which is not energy efficient and environmental friendly. Another shortcoming of carbothermic reduction is that, it is unable to preserve the original morphology of the precursors, because the reaction temperature over 2000 ºC is higher than the melting point of silicon (1414 ºC). However, as we mentioned before, nanoscale silicon materials with porosity is the desired anodes for LIBs, which can accommodate the volume expansion and strain during lithiation.

Magnesiothermic reduction is another route which can offer a facile method for synthesis of crystalline and porous silicon at moderate temperature (>650 ºC). This method has been proved to be able to preserve the morphology of precursors as small as 15 nm. Magnesiothermic reduction of silica as in Equation, happens at or slightly above the melting point of magnesium (650 ºC)[4]:

$$2Mg(g) + SiO2\ (s) \rightarrow Si(s) + 2MgO\ (s)$$

The products, magnesia can be removed by HCl very easily. The product of acid-treatment, $MgCl_2$, can be recycled to magnesium via electrolysis[5]. However, there is a possible unwanted byproduct Mg_2Si, which will reduce the yield of silicon. The side reaction is shown below:

$$Mg\ (g) + Si\ (s) \rightarrow 2Mg_2Si\ (s)$$

The formation of Mg_2Si will also affect the morphology of silicon when silicon products are immersed in HCl to remove MgO due to its solubility in HCl, as bellow:

$$MgO\ (s) + 2HCl\ (l) \rightarrow MgCl2\ (aq) + 2H_2O\ (l)$$

$$Mg_2Si\ (s) + HCl\ (l) \rightarrow SiH4\ (g) + 2MgCl_2\ (aq)$$

$$SiH_4 + O_2\ (g) \rightarrow SiO_2\ (s) + 2H_2O\ (g)$$

The products of silane are flammable, burning in air spontaneously, to form SiO_2. The whole procedure of magnesiothermic reduction is illustrated in Fig. 2.2[6]. Fortunately, the formation of $MgCl_2$, generally happens when the moral ratio of Si : Mg is at 1: 2 or lower.

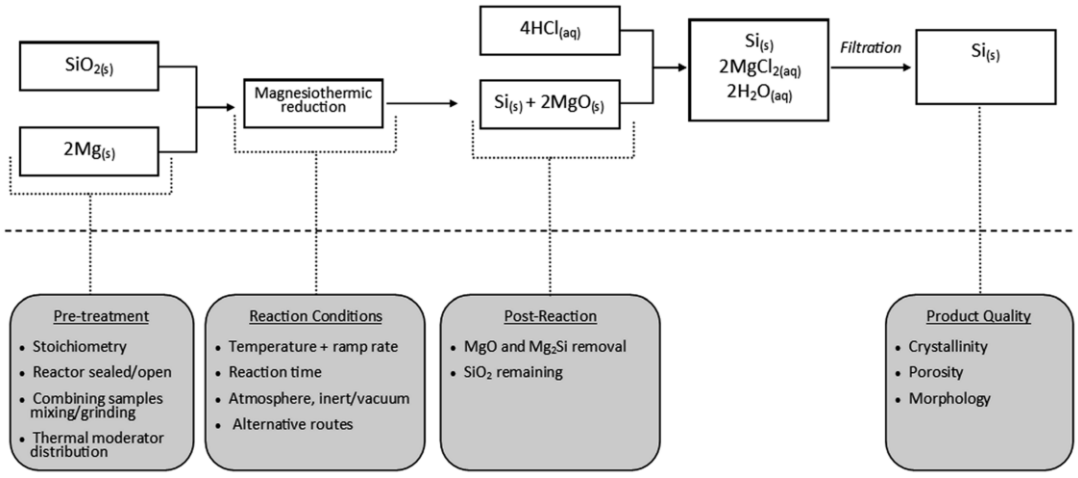

Fig.2. 2 Scheme Desinged for Magnesiothermic Reduction

As mentioned in Fig. 2.1 and Fig. 2.2, the precursor or silica is the very first step for magnesiothermic reduction, and the morphology of silica will be preserved during

reduction. Hence, the parameter of the silica is very important. Silica from precursors, such as sands, rice husks, have nonuniform structures morphologies, will lower the performance of silicon anodes reduced from them. Herein, the stöber method can be applied to achieved designed uniform morphologies. The stöber method was proposed by Werner Stöber in 1967 to grow spherical silica particles of uniform size[7]. It was originally done by hydrolysis of alkyl silicates and subsequent condensation of silicic in alcoholic solutions with catalyst of ammonia[7,8]. In our work, according to our experience, we use TEOS as a replacement for alkyl silicate.

2.2 Experiment

2.2.1 Synthesis of Monodisperse Solid Silica Spheres (SS) via Modified Stöber Method

To begin with, 9 ml NH_3H_2O, 16.25 ml ethanol, 24.75 ml DI water are mixed at room temperature at a stirring velocity of 450 rpm to form a uniform basic solution A. 4.5 ml TEOS is added into 45.5 ml ethanol to form solution B and the solution is stirred at 450 rpm for couple minutes to be well mixed. The solution B is poured into solution A very quickly while stirring at 450 rpm and the final mixture is kept stirring for 2 hours. Lastly, the solution with suspending SiO_2 particles are collected by centrifuging and repeatedly washed with DI water and ethanol. Silica monodisperse spheres can be achieved after overnight vacuum dried.

2.2.2 Synthesis of Monodisperse Silicon Spheres via Magnesiothermic Reduction

Monodisperse porous silicon nanospheres (MPSSs) are prepared via morphology preserved magnesiothermic reduction. Firstly, produced SS powders are mixed with NaCl in a 1:10 w/w and then the SS/NaCl mixture is dissolved in deionized water while stirring at 450 rpm at room temperature for 3 hours. The solution with mixed SS/NaCl powders is aged at 100 ºC to remove all water. Then the dried SS/NaCl powders are ball milled and mixed with Mg powder (99.5%, -325 mesh, Sigma-Aldrich) in a 1:0.9 w/w SS: Mg ratio. The powder is loaded into SS 316 Swagelok-type reactors at an inert environment in an argon-filled VAC Omni-lab glovebox (0.5 ppm H_2O, 0.15 ppm O_2) to make sure no air left in the mixed powder to lower the yield of silicon. After that, the reactors with reactants are loaded into an MTI GSL-1200X quartz tube furnace at an Argon flow of 200 sccm. The furnace is heated to 700 ºC at a rate of 5 ºC/min, held at 700 ºC for 0.5 hours, 1 hour, 3 hour, 6 hours, 10 hours and 12 hours, separately. When the procedure is done, the whole system is cooled to room temperature purged with Argon. The resulting product is then washed with DI H_2O several times to remove NaCl. Unwanted Mg_2Si and MgO is removed via etching in 2 M HCl overnight and residual SiO_2 is removed by etching in 5% HF for 1 hour. The powder is washed several times with DI H_2O, dispersed in ethanol, and dried at 100 ºC under vacuum overnight.

2.2.3 Carbon Coating of MPSSs (MSNSs) in CVD

The product from last step, MPSSs are loaded in a quartz boat and transferred into a CVD furnace purged with Argon. When the air pressure reaches 700 Torr, MPSSs are heated to 900 ºC in an Ar/H_2 atmosphere at a flow rate of 200 sccm and 30 sccm,

separately. Once the temperature reaches 900 ^{o}C, acetylene (C_2H_2) is introduced to trigger and continue the growth of carbon layer at a rate of 30 sccm.

2.2.4 Material Characterization

The morphology is examined by scanning electron microscopy (SEM, FEI NNS450). The phase identification and purity are characterized by R-ray diffraction (XRD, PANalytical Empyrean) with Cu-Kα radiation.

2.3 Results and Discussion

Stober method, can produce monodisperse, spherical SiO_2 particles via the ammonia-catalyzed reactions of tetraethylorthosilicate (TEOS) in an ethanol solvent with water[9]. The diameter of silica spheres can be from 5 to 2000 nm by varying concentration of ammonia, water and ethanol[9-10]. The reactions are shown as bellow:

$$Si(OR)_4 + H_2O \rightarrow OH^-(OR)_3Si(OH) + ROH$$

$$(RO_3)Si(OH) + H_2O \rightarrow SiO_2\downarrow + 3ROH$$

The morphology and size of our as-prepared silica particles are shown in Fig. 2.3. It shows that, the monodisperse silica spheres are synthesized via a facile route without any additives or special treatment. The uniform distribution of silica spheres with diameters around 300 nm make it an ideal precursor for preparation of monodisperse silicon nanoparticles via magnesiothermic reduction.

The key paraments to control the magnesiothermic reduction are: reaction time, temperature, temperature ramp rate and molar ratio of different reactants. Either of them has the possibility to influence the morphologies of as-reduced silicon materials. Firstly,

fast temperature ramp rate of 40 ºC/min can produce silicon products with smaller surface area and macropores due to the ununiform heat distribution and local reactions, according to Liu et.al[11]. With the above consideration in mind, we apply a slower ramp rate of 5 ºC/min here. Additionally, any temperature higher than melting point of 690 ºC can be applied in the magnesiothermic reduction. Barati et. al[12] indicates that, when the reduction is operated

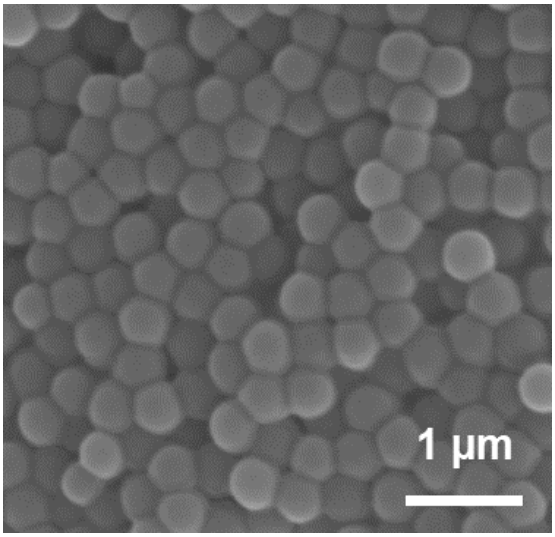

Fig.2. 3 SEM Images of Silica Spheres

during750 ºC and 900 ºC, there is little effects on the yield of silicon products. However, Xie et. al[13] shows that there are more $MgSO_4$ formed as the temperature increased from 700 ºC to 900 ºC. In consideration of energy saving issue and prevention of the unwanted byproduct, $MgSO_4$, we choose 700 ºC as the reduction temperature, where cooperation of

NaCl acts as a heat cavenger to keep the reaction temperature rise at 801 °C to prevent the fusion of silicon nanospheres. The magesiothermic reduction is illustrated in Fig. 2.4[14]. Moreover, to further study the effect of different reaction time on morphologies and yield of silicon products. All the silica precursors are mixed with Mg at a weight ratio of

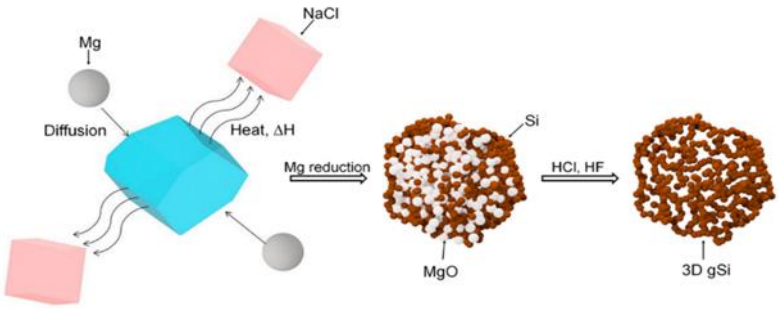

Fig.2. 4 Schematic of the Mg reduction process using NaCl as heat scavenger[14]

Table 2.1 Yield of Silicon Products with Varying Reduction time

Sample #	Reduction Time	Acid Treatment After Reduction		Yield of Silicon (% of Theoretical Value)
1	0.5 hours	2 M HCl Washing	5 % HF Etching	~50%
2	1 hour			~70%
3	3 hours			~90%
4	6 hours			~90%
5	10 hours			~90%
6	12 hours			~90%

Mg/SiO_2 = 0.9/1 (w/w), and hold at 700 °C for various time, from 0.5 to 12 h. The yields of silicon products via different reduction time are shown in table 2.1. The results show that the Si yield increases from 55% at 0.5 h to 90% at 3.0 h and then tends to a plateau for longer time. The increases in the Si yield is associated with further completion of the reduction reactions that are controlled by solid state diffusion at some stages. There is no significant improvement for the yield of silicon products reduced for extending reduction time beyond 3 h, due to the near complete reduction of SiO_2 within the first 3 h.

The morphologies of silicon products reduced by different reduction time are also checked by SEM, shown in Fig. 2.5. Clearly, the spherical nature is perfectly preserved from silica precursors to silicon products, which confirms the morphology preservation ability of magnesiothermic reduction. Besides, there is very slightly difference in surface morphologies of silicon samples reduced by 3 hours or longer, which is consistent with the results of yield. It further verifies the reduction of silica completed in the first 3 hours. The mesopores are achieved by the removal of MgO/Mg_2Si in the surface[15]. There are macrospores on the surface of silicon which is held at 700ºC for 0.5 h. We believe that, these different macropores is due to the removal of unreacted SiO_2 etched by HF. As mentioned above, the yield of silicon products is around 50% of theoretical value, which means SiO_2 is not completely reduced via magnesiothermic reduction. The unreacted SiO_2 is removed by HF, leaving macropores on the surface. As the reduction time gradually increased, the silica is further reacted to magnesium till near completion occurs at 3 hours. Accordingly, there are mostly MgO left on the surface of silicon spheres,

which can be removed by HCl to form mesopores. When the reduction time is increase further, the morphologies of silicon spheres are slightly changed due to the same reaction inside the reactor.

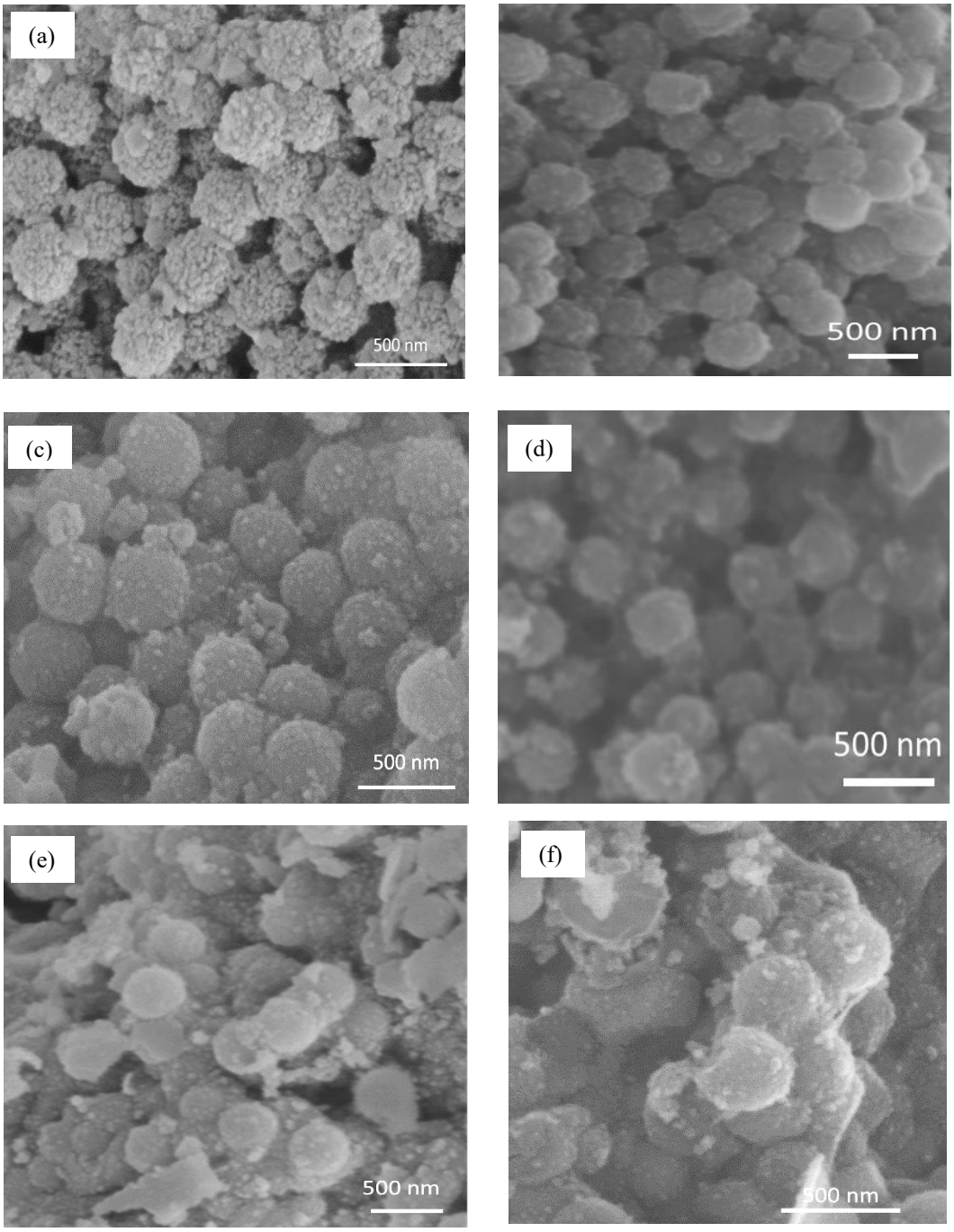

Fig.2. 5 EM image of MPSSs Reduced by Varying Reduction Time. (a) 0.5 h, (b) 1h, (c) 3h, (d) 6h, (e) 10h, (f) 12h

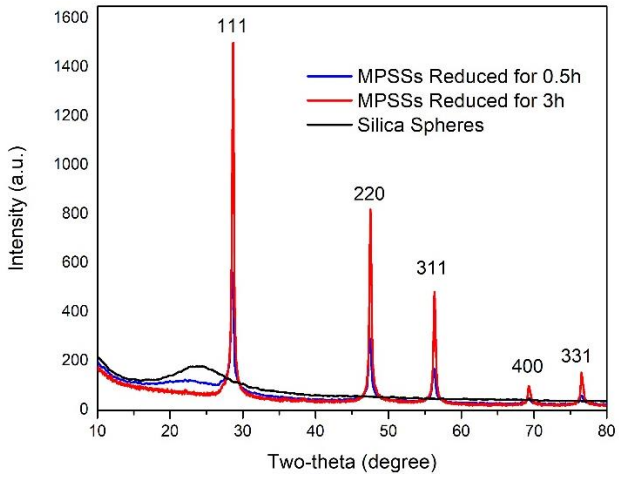

Fig.2. 6 XRD Spectra of Silica Spheres (SS), Monodisperse Porous Silicon Spheres (MPSSs) Reduced for 0.5h and 3h

The phases of silica spheres (SS), and monodisperse porous silicon spheres are checked by X-ray diffraction (XRD), in Fig. 2.6. The spectrum exhibited by MPSSs reduced for 3h and 0.5h shows sharp peaks without amorphous scattering, suggesting the formation of high degree crystallinity of Si. The peaks at 2θ of 28.8°, 47.8°, 56.7°, 69.7° and 77.1° represent (111), (220), (311), (400) and (331) planes, respectively. The wide and small peak around 25° of the spectra exhibited by MPSSs reduced for 0.5h represents the residual SiO_2, which indicates the considerable amount of unreacted SiO_2 for reduction time of 0.5h.

2.4 Conclusion

In this work, we studied the morphologies and yields of silicon products via stöber method and magnesiothermic reduction for varying time. A facile modified stöber method is used to synthesis submicron monodisperse silica spheres with diameter of 300

nm. Then, the spherical nature is perfectly preserved from silica to silicon by magnesiothermic reduction. Moreover, we find that, when the operation time for magnesiothermic reduction is increased from 0.5 h to 3 h, the yield of silicon products is increased from 50 % to 90%. When the reduction time is longer than 3 h, there is a plateau for the yield indicating the near completion of reduction in 3 hours. Additionally, there are large macropores in the surface of silicon nanospheres reduced for 0.5 h due to the removal of lots unreacted SiO_2. In the following work, we will study how other parameters of magnesiothermic reduction can influence the electrochemical performance of monodisperse silicon based anodes for LIBs.

2.5 Reference

1. Khalafalla, S. E. & Haas, L. A. Kinetics of Carbothermal Reduction of Quartz Under Vacuum. J. Am. Ceram. Soc 55, 414-417 (1972).

2. Hutchison, S. G., Richardson, L. S. & Wai, C. M. Carbothermic reduction of silicon dioxide- a thermodynamic investigation. Metall. Mater. Trans. B 19, 249-253 (1988).

3. Reeves, C. E. e. a. Potential for photochemical ozone formation in the troposphere over the North Atlantic as derived from aircraft observations during ACSOE. J. Geophys. Res 107, ACH 14-11 -ACH 14-14 (2002).

4. Smith, J. & Smythe, R. Vapor pressure measurements over calcium, magnesium and their alloys and the thermodynamics of formation of CaMg 2. Acta Metallurgica 7, 261-267 (1959).

5. Kipouros, G. J. & Sadoway, D. R. The chemistry and electrochemistry of magnesium production. Adv. Molt. Salt Chem. 6, 127-209 (1987).

6. J. Entwistle, A. Rennie and S. Patwardhan, A review of magnesiothermic reduction of silica to porous silicon for lithium-ion battery applications and beyond, J. Mater. Chem. A, 6, 18344 (2018).

7. W. Stober, A. Fink, Controlled Growth of Monodisperse Silica Spheres in the Micron Size RangeJour. Colloid Interface Sci. 26, 62--69 (1968)

8. W. Wang, Z. Favors, R. Ionescu, R. Ye, H. H. Bay, M. Ozkan, C. S. Ozkan, Monodisperse Porous Silicon Spheres as Anode Materials for Lithium Ion Batteries, Scientific Rep., 5, 8781 (2015).

9. Werner Stöber, A. F., Controlled Growth of Monodisperse Silica Spheres in the Micro Size Range. Journal of Colloid and Interface Science, 26, 62-69 (1968).

10. G.H. BOGUSH, M.A. TRACY and C.F. ZUKOSKI IV, Preparation of Monodisperse Silica Particles: Control of Size and Mass Fraction, Jour. Non-Crystalline Solids, 104, 95-106 (1988).

11. N. Liu, K. Huo, M. T. McDowell, J. Zhao and Y. Cui, Rice husks as a sustainable source of nanostructured silicon for high performance Li-ion battery anodes. Sci. Rep., 3, 1 (2013).

12. K. K. Larbi, M. Barati and a. McLean, Reduction behaviour of rice husk ash for preparation of high purity siliconCan. Metall. Q., 50, 341 (2011).

13. J. Xie, G. Wang, Y. Huo, S. Zhang, G. Cao and X. Zhao, Nanostructured silicon spheres prepared by a controllable magnesiothermic reduction as anode for lithium ion batteries. Electrochim. Acta, 135, 94 (2014).

14. C. Li, C. Liu, W. Wang, Z. Mutlu, J. Bell, K. Ahmed, R.Ye, M. Ozkan and C. S. Ozkan, Silicon Derived from Glass Bottles as Anode Materials for Lithium Ion Full Cell Batteries, Sci.Rep., 7, 917 (2017).

15. Bao, Z.; Weatherspoon, M. R.; Shian, S.; Cai, Y.; Graham, P. D.; Allan, S. M.; Ahmad, G.; Dickerson, M. B.; Church, B. C.; Kang, Z.; Abernathy, H. W., 3rd;

Summers, C. J.; Liu, M.; Sandhage, K. H., Chemical reduction of three-dimensional silica micro-assemblies into microporous silicon replicas. Nature, 446, 172-5 (2007).

Chapter 3 Scalable Coral-Like Si Powders with Three-Dimensionally-Interconnected Structures as Lithium Ion Battery Anodes

3.1 Introduction

As the increased demand of electronic devices, electrical vehicles and so on, more powerful energy storage devices are needed. Lithium ion battery (LIB) is the most promising energy storage device because of its higher energy density and lower self-discharge rate. However, the capacities of most widely used electrode materials are very limited. The most widely used commercial anode, graphite, has a low theoretical specific capacity of 372 mAh g^{-1}. To meet the demand of more powerful LIBs, people have been studying new anode materials. Silicon is considered as one of the most promising potential anode materials because of its high abundance, low cost and high theoretical specific capacity. Silicon has a theoretical capacity of 3572 mAh g^{-1} corresponding to the phase of $Li_{15}Si_4$ at room temperature[1,2]. However, there are some challenges to prevent the commercial application of Si anodes: extremely high volume-expansion and the instinct of low electron conductivity. The volume expansion of 300% will introduce the mechanical stress which can cause the fracture and the pulverization of Si anodes[3]. It can further disconnect silicon active materials and the current collector. Besides, the volume expansion will prevent formation of stable SEI, the continuous SEI process will lead extra Li^+ consumption and electrolyte decomposition[4,5].

Researchers have demonstrated that, Si anodes with nanostructures have better cycling stabilities, whose void spaces can accommodate the volume expansion and large strains without pulverization[6]. Additionally, Liu et.al indicated there is a critical dimeter of 150 nm, beyond which, the Si anodes will fracture or pulverize[7]. The instinct low conductivity of silicon can also be solved by carbon/silicon composites[8] and conductive coating such as metal coating[9] or polymer coating[10].

In this work, we synthesized coral-like porous Si powders with a three-dimensionally-interconnected structure via a low cost, facile and scalable method. The porosity of the Si nanospheres can accommodate the volume expansion and release strain-stress within structure during lithiation and delithiation process, respectively. Moreover, the coral-like and interconnected structure offers shorter Li^+ diffusion path to achieve a higher conductive silicon anode.

3.2 Experiment

3.2.1 Material Synthesis

Solid silica chunks were synthesized by the modified Stöber Method. Firstly, EtOH: TEOS (mol:mol=2:1) were premixed via vigorous stirring to form solution A. Secondly, Solution B was prepared from H_2O: HCl = 200:1 (mol:mol). Solution B was dropped into solution A via stirring at 450ppm to produce the final solution which would be stirred for 2 hours. The resulting solution was aged at 70 ^oC under vacuum to be completely dried and form SiO_2 chunks. Milled SiO_2 chucks were immersed into DI water and sonicated. After settled down for a while, the solution was layered. The top solution was collected, washed and dried.

The resulting products, SiO_2 nanosized spheres were milled and mixed with NaCl in a 1:10 w/w ratio and the mixed powders were dissolved in DI H_2O. Next, the vigorously stirred solution was dried at 100 ºC overnight. Then, collected powders were put into the Swagelok reactor with Mg in a weight ration of SiO_2: Mg = 1:0.83. The reactor was sealed in the glove box filled with Ar and loaded to a furnace. The furnace, purged with Ar, was heated to 700 ºC at a rate of 5 ºC/min, held at 700 ºC for 2 hours and cooled to room temperature afterwards. The resulting products were washed by DI water and HCl to remove NaCl and by-products (MgO), respectively.

The carbon coated Si nanosized materials were produced in furnace. The Si nanosized powders were loaded in a quartz boat and placed in the center of quartz tube furnace purged with Ar. The furnace was heated to 950 ºC in 15 mins with H_2 at a flow rate of 30 sccm at 700 Torr. Acetylene (C_2H_2) was then introduced to achieve the C-coating across Si surfaces at 950 ºC for 15 minutes. Then the system was naturally cooled down.

3.2.2 Material Characterization

The morphology was characterized by scanning electron microscopy (SEM, FEI NNS450) and transmission electron microscopy (TEM, Titan Themis 300). The phase identification was examined by R-ray diffraction (XRD, PANalytical Empyrean) with Cu-Kα radiation. The Raman spectroscopy was carried to check the purity of Si powders with a 532 nm excitation laser (8 mW excitation power, 100X objective lens).

3.2.3 Electrochemical Measurements

The Si anode was prepared by a slurry composed of 70% active material (C), 20% PAA binder and 10% acetylene black. Batteries with half-cell configuration were assembled in an Argon-filled VAC Omni-lab glovebox with oxygen and H_2O level below 1 ppm. The solution comprising 1 M $LiPF_6$ in FEC/DMC (1:1, v/v) was used as the electrolyte with a counter electrode of lithium metal and a Celgard 3501 porous PP membrane as the separator. Electrochemical performance and galvanostatic charge/discharge were conducted on Arbin BT300 with a voltage window ranging from 0.01 to 1.0 V (vs. Li^+/Li), while electrochemical impedance spectroscopy (EIS) was performed on the Biologic VMP.

3.3 Results and Discussion

3.3.1 Structural Characterization of Coral-Like Si Powders

Monodisperse silicon nanoparticles can be synthesized by base-catalyzed Stöber method[11] and magnesiothermic reduction[12]. The conductivity of monodisperse silicon nanoparticles are very limited and their diameters are larger than the critical diameter of 150 nm[12]. To achieve an three dimensionally interconnected silicon nanoparticles, we applied acid-catalyzed method other than base-catalyzed one. Under acid environment, TEOS tends to polymerized into cross-linked and interconnected structures instead of monodisperse spheres[11, 13]. The morphology of our as-prepared Si powders was studied by SEM in Fig. 1. Clearly, spherical shape with diameter around 100 nm had been preserved during the conversion from SiO_2 to Si[12]. Simultaneously, the Si nanosized

powders (SiNPs) also exhibited typical three-dimensionally interconnected and coral-like structures.

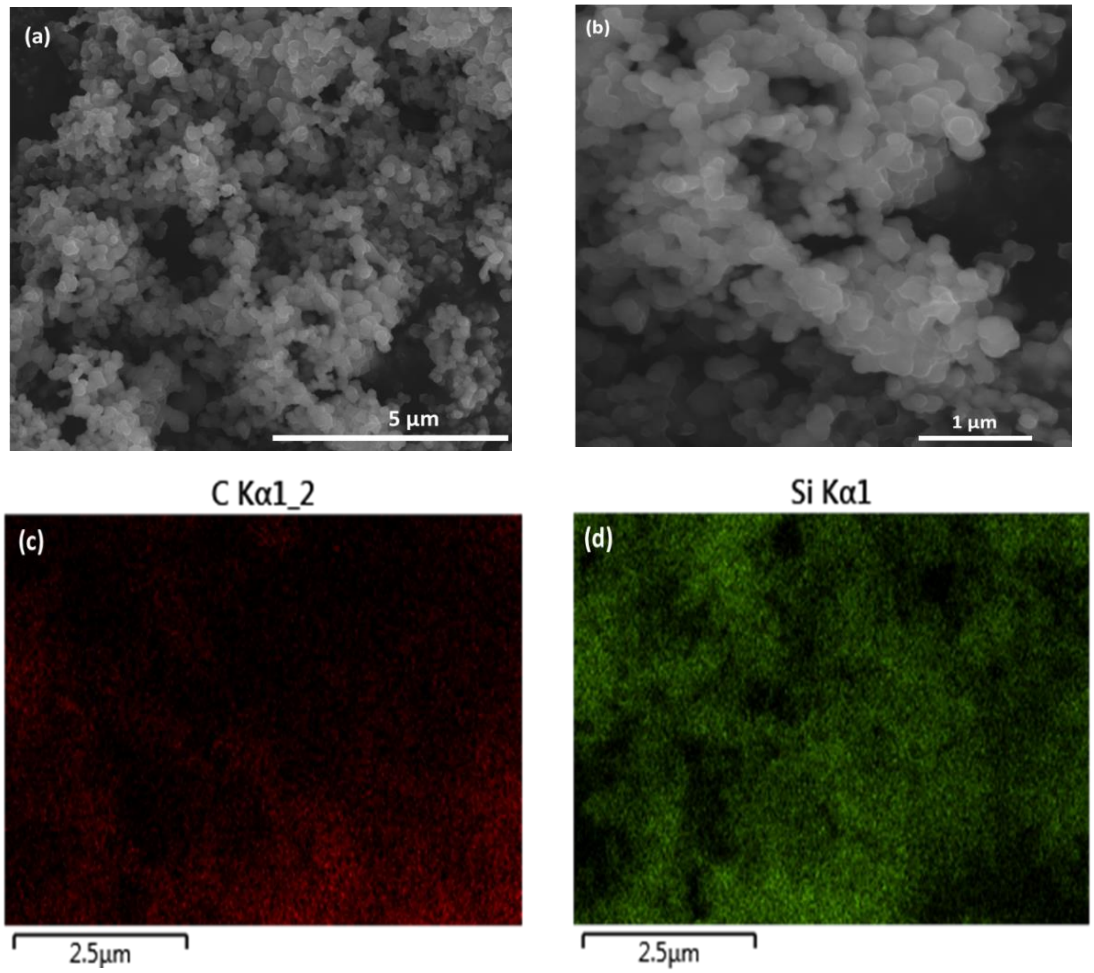

Fig.3. 1 SEM Images of 3D-SiNPs, (c)& (d) EDX mapping of carbon coatind 3D-SiNPs

The high porosity of the 3D-SiNPs were verified by Brunauer-Emmett-Teller (BET) surface area measurements, which demonstrated a high specific surface area of 127.56 m^2g^{-1} and calculated average diameter of 10.21 nm, as in Fig. 2. The inset image revealed a pore diameter distribution with a peak centered at 25 nm indicating a considerable amount of pores with diameters of 25 nm. The higher surface area and pore volume distribution indicated the existence of larger internal porosity compared to monodisperse silicon nanoparticles[12a]. The high porosity was introduced by the removal of byproducts ($MgO/MgCl_2$) via acid-treatment[14]. The 3D-SiNPs comprised a highly porous three-dimensional (3D) network of interconnected silicon nanoparticles with diameters ~100nm. The interconnected structures provide the path for charges (Li^+ and electrons) transferring while the porous nature and high surface area can accommodate

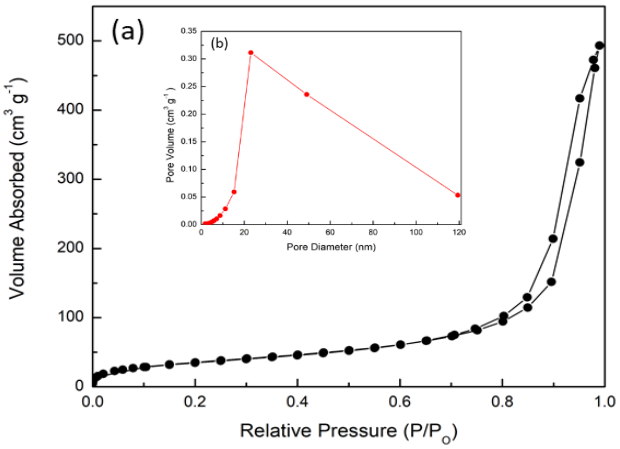

Fig.3. 2 BET Surface Area Measurement of Silicon Cluster with N_2 Sorption(b) Distribution of Pore Diameters

volume expansion and release stress during lithiation, respectively. Additionally, with the accommodated volume expansion of lithiated Si anodes, the SEI was well preserved to lower the consumption of Li^+ and decomposition of electrolytes. The interconnected porous structure not only was available for volume expansion buffering, also could minimize capacity fading due to SEI layer degradation and low conductivity.

The phase of SiNPs was also examined by X-ray diffraction (XRD) in Fig.4 (a). The spectrum demonstrated sharp peaks without amorphous scattering, respect to the formation of high degree crystallinity of Si. The peaks at 2θ of 28.8°, 47.8°, 56.7°, 69.7° and 77.1° were associated to (111), (220), (311), (400) and (331) planes, respectively. The composition, purity and phase of SiNPs were further verified by Raman spectroscopy. The sharp peak at 514.5 cm^{-1} indicated the relatively high-purity of Si clusters in Fig. 3 (b).

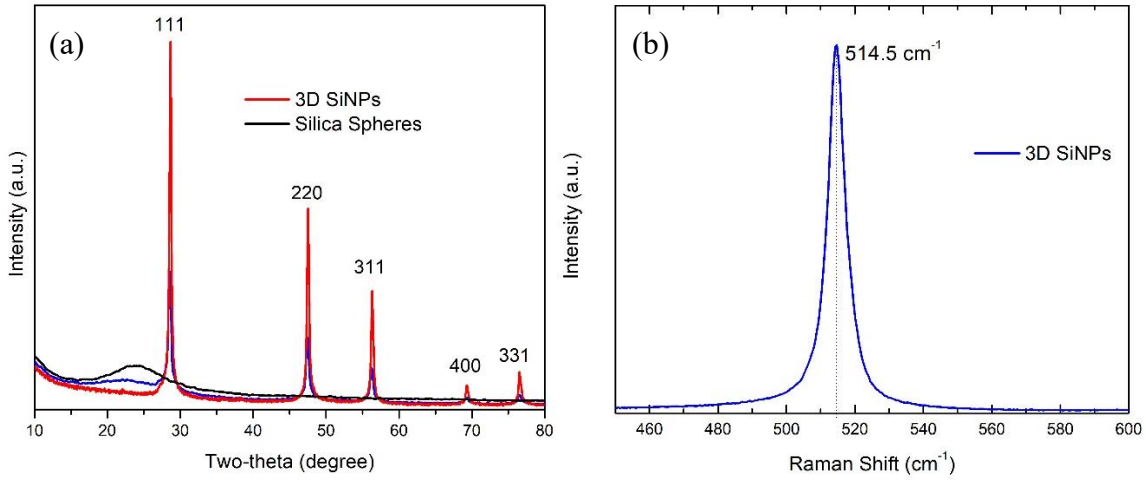

Fig.3. 3 (a)Raman Spectra, (b) XRD Spectra

Despite the path provided by the interconnected structures, the low conductivity of Si still limited its fast cycling capability and capacity. To further improve the conductivity of 3D-SiNPs, a conformal amorphous carbon coating was introduced across all surfaces of 3D-SiNPs via CVD. The weight ratio of Si : C was ≈80:20, which was calculated by the weight variation before and after carbon coating. The morphology of 3D-interconnected carbon coated Si nanoparticles (3D-CSiNP) was further studied in a transmission electron microscopy. High resolution TEM analysis revealed that SiNPs were coated by thin carbon layers with thickness ~ 15 nm as shown in Fig. 4 (b). HRTEM of 3D-CSiNP clearly showed the uniform distribution of carbon coating surrounding 3D-SiNPs, verifying the successful deposition of the conformal carbon layer.

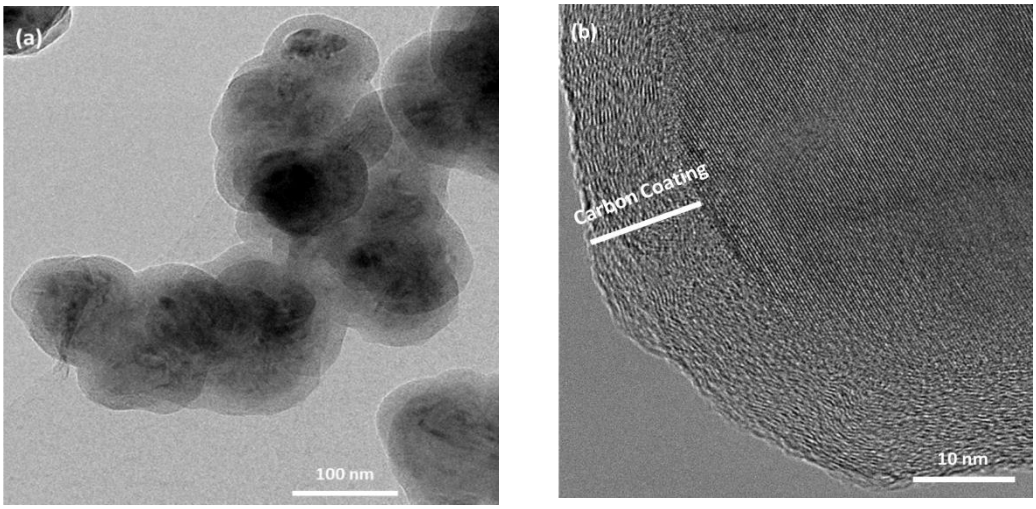

Fig.3. 4 TEM images of 3D-CSiNPs displaying the conformal carbon coating and the carbon layer thickness across surfaces of 3D-SiNPs with (a) low magnification and (b) high magnification

3.3.2 Electrochemical Performance of Coral-Like Si anode

Cyclic voltammetry (CV) was tested in a voltage window from 0.01 to 1.5 V (vs. Li^+/Li), with a scan rate of 0.1 mV sec^{-1} in Fig. 5(a). The peaks around 0.18 V were associated with lithiation while peaks at 0.39 V and 0.54V were corresponded to delithiation. All peaks increased and coincided after 10 cycles, signifying a gradual formation of stable SEI layers. To verify conformal C-coating as an effective strategy to improve cycling stability and columbic efficiency, cycling performance of 3D-CSiNP anodes and 3D-SiNP anodes were examined as shown in Fig. 5 (b). The 3D-CSiNP electrodes showed a higher capacity over that of 3D-SiNP electrodes, which suggested the substantial enhancement of carbon coatings on stabilities of Si anodes. At the initial cycles with rates of 40/C, 20/C and 10/C, a stable SEI layer was formed, as confirmed by

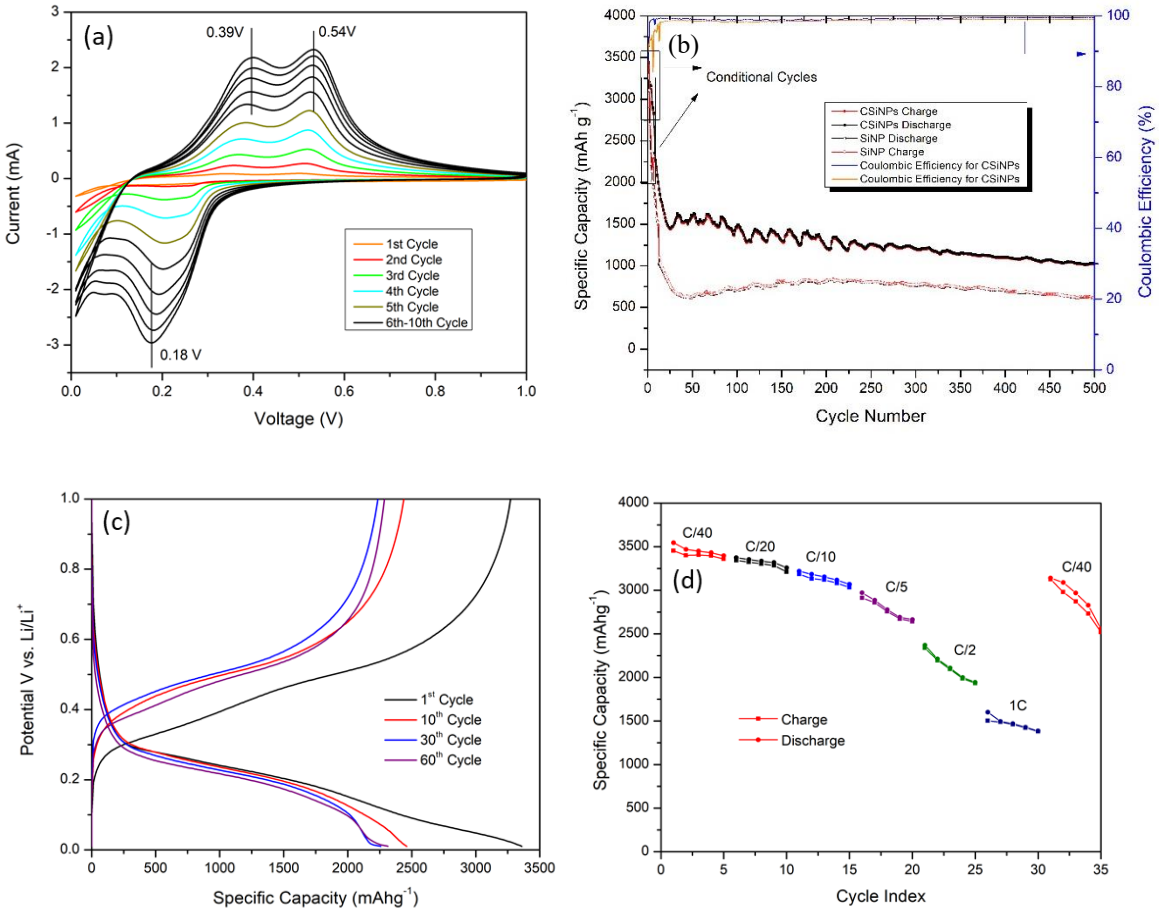

Fig.3. 5 Figure 5 (a) Cyclic voltammetry characteristic of Si@C cluster anodes. Scan rate: 0.05 mV sec−1. (b) Cycling performance and Coulombic efficiency of Si@C anodes at a current density of C/2. (c) The corresponding galvanostatic charge-discharge profles of 3D-SiNPs based half-cell. (d) C-rates cycling performance of 3D-CSiNP electrodes

CV measurements. After the kinetic enhancement in the conditional cycle at low current densities, the 3D-CSiNP anodes were cycled at a high C-rate of C/2 and exhibited a reversible capacity of ~1018 mAh g^{-1} with capacity retention of 43% (Coulombic efficiency of >99%) at 500th cycles. In comparison, non-carbon coated SNP electrodes presented capacity of 608 mAh g^{-1} with capacity retention of 30% (corresponding to Coulombic efficiency of 98%) after the same cycling process at same rate. This performance difference between 3D-CSiNP and 3D-SiNP anodes was mainly due to the increased conductivity of 3D-CSiNPs, which enable sufficient charge transfer between active materials and the micro-level acetylene black within the electrode. Moreover, the carbon coating surrounding 3D-SiNPs improved the cycling stability of anodes, which was confirmed by the higher capacity retention and coulombic efficiency of 3D-CSiNP anodes over 500 cycles. The cycling performance of 3D-CSiNP electrodes were comparable to several reported Si anodes via magnesiothermic reduction. The profile of charge-discharge at 1^{st} and 10^{th} cycles were in good agreement with the peaks of CV plots in Fig. 5 (a) and Fig. 5 (c). Rate capability of CSiNP anodes was demonstrated with different current densities measured at various rate in Fig 6 (d).

To further investigate the electrochemical performance of the 3D-CSiNP anode, EIS (Electrochemical Impedance Spectroscopy) was implemented among the cycles (10mV sinusoidal signal, frequency 10mHz-10kHz), then an equivalent circuit (Figure 6), which had been proved to be appropriate for many lithium-ion battery systems[15], was used to fit the experimental data. ESR (Equivalent series resistance) or R_s, mainly represents the ionic impedance of the electrolyte, as well as the ohmic part of the

electrode impedance while $R_{SEI+INT}$ comprise the impedance caused by the SEI layers, imperfect contact due to the cell configuration. R_{CT} is associated to the redox reactions at the interface of the electrode and electrolytes during the lithiation and delithiation process. CPE_W (Constant Phase Element) can characterize the diffusion of the lithium ions in the electrolyte and the electrode.

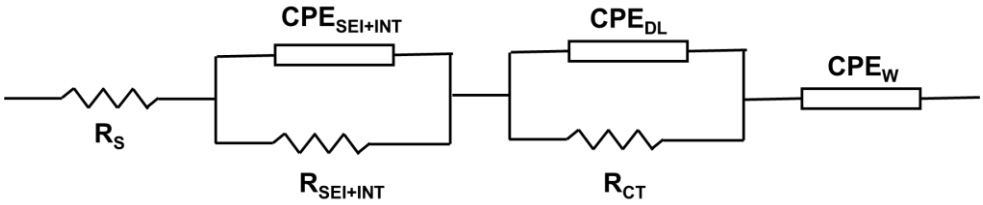

Fig.3. 6 Equivalent Circuit for fitting

Experimental and fitting plots are shown in Figure 7. The EIS results at fully charged states at rate of C/40, C/20, C/10 and C/5 were illustrated in Fig. 7 (a)-(d), respectively. The fitting plots were in a good alignment with the experimental ones. Compared with some previous nanosized silicon anodes[15b, 16] and the monodisperse silicon nanoparticles[5, 12a], the impedance of 3D-CSiNP anode was very small, which indicated that 3D-CSiNPs had a much better conductivity than others.

The decreased R_e in initial 2 cycles indicated that for high surface area electrode, more surface area of active materials was activated during the cycling process. In Fig. 7(b), the increased R_e was associated to the formation of SEI layers. When the cell was cycled at a higher rate of C/10, the increased impedance represented the break of well-formed SEI layers and side reactions occurred simultaneously to form new SEI layers. The above analysis was confirmed by the behavior of ESR and Q_w values in Fig. 8. When

cells were cycled at low rates of C/40, C/20, C/10, the ESR increased continuously, suggesting the consumption of the electrolyte to form SEI layers. Moreover, the value of Q_w kept decreasing, representing growth of the diffusion length which was caused by the thicker SEI layers over cycles. At a higher rate of C/5, the behavior of ESR, RCT and RSEI+INT signified that the new stable SEI layers was gradually formed.

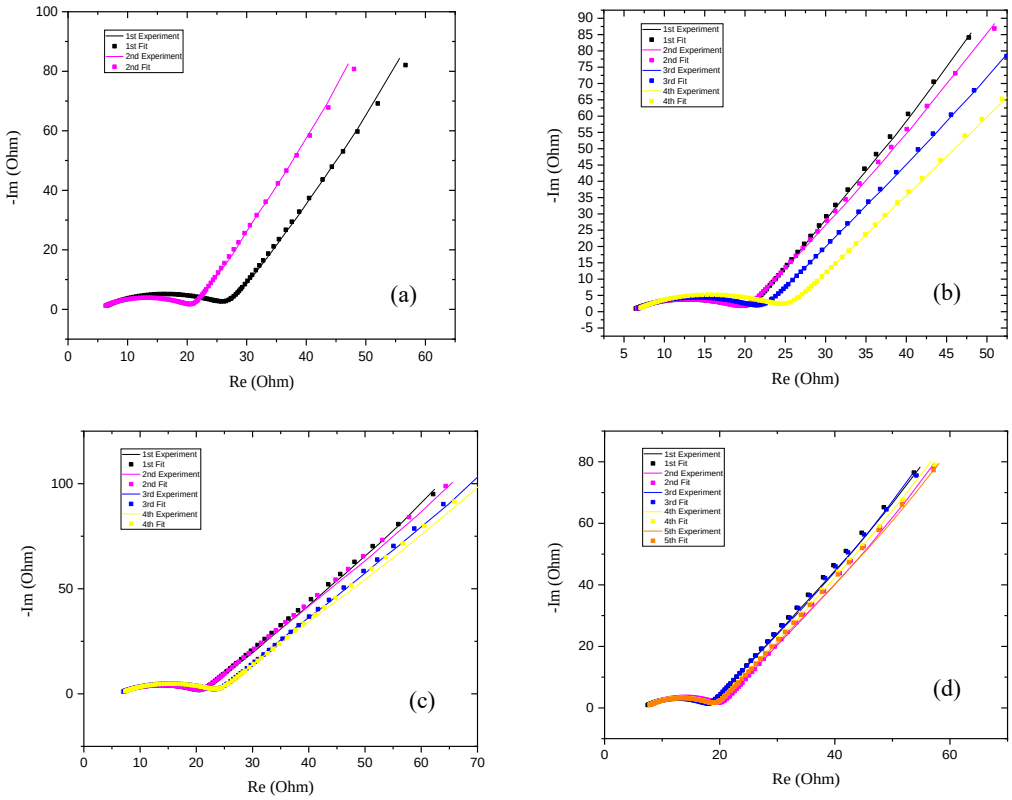

Fig.3. 7 EIS experimental and fitting plots for a) C/40 cycles; b) C/20 cycles; c) C/10 cycles;

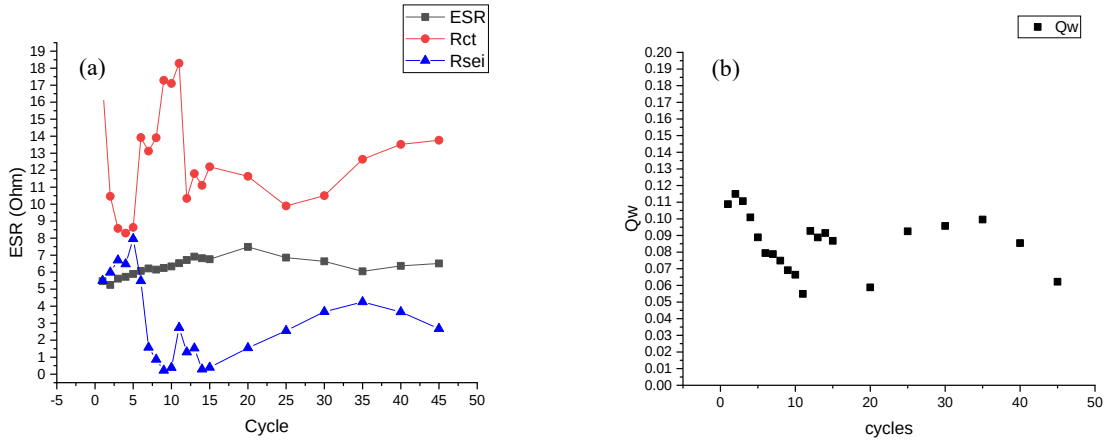

Fig.3. 8 (a)Key impedance values; (b)Diffusion capacitance

3.4 Conclusion

In conclusion, synthesis of coral-like interconnected porous Si and C nanocomposite spheres via a facile magnesiothermic reduction with subsequent CVD process has been demonstrated. The excellent electrochemical performance of 3D-CSiNP anodes can be mainly attributed to the mitigated volume expansion and improved system conductivity resulting from high porosity, high surface area, the interconnected network of Si nanoparticles and the conformal carbon coating. The porous structure allow the stress released within the structure without any mechanical fracture and pulverization during lithiation/delithiation, while the 3D interconnected nature provide the path for electrons and lithium ions transferring. Half cells with anodes based on 3D-CSiNPs demonstrate a higher reversible capacity of 1018mAh g^{-1} after 500 cycles, indicating an

enhanced cycling stability. We believe optimization and further development of this 3D-CSiNP anode design will lead to new opportunities for high energy density energy LIBs.

3.5 Reference

1. Changling Li, C. L., Wei Wang, Jeffrey Bell, Zafer Mutlu, Kazi Ahmed,Rachel Ye, Mihrimah Ozkan and Cengiz S. Ozkan, *Towards flexible binderless anodes: silicon/carbon fabrics via double-nozzle electrospinning*. Chemical communications**, 52**, 11398-11401, (2016).

2. Li, C.; Liu, C.; Wang, W.; Mutlu, Z.; Bell, J.; Ahmed, K.; Ye, R.; Ozkan, M.; Ozkan, C. S., *Silicon Derived from Glass Bottles as Anode Materials for Lithium Ion Full Cell Batteries*. Scientific reports, **7**, 917 (2017).

3. Zeng, Z.; Liu, N.; Zeng, Q.; Lee, S. W.; Mao, W. L.; Cui, Y., *In situ measurement of lithiation-induced stress in silicon nanoparticles using micro-Raman spectroscopy*. Nano Energy, **22**, 105-110 (2016).

4. Wu, H.; Chan, G.; Choi, J. W.; Ryu, I.; Yao, Y.; McDowell, M. T.; Lee, S. W.; Jackson, A.; Yang, Y.; Hu, L.; Cui, Y., *Stable cycling of double-walled silicon nanotube battery anodes through solid–electrolyte interphase control*. Nature Nanotechnology, **7**, 310 (2012).

5. Wang, W.; Favors, Z.; Li, C.; Liu, C.; Ye, R.; Fu, C.; Bozhilov, K.; Guo, J.; Ozkan, M.; Ozkan, C. S., *Silicon and Carbon Nanocomposite Spheres with Enhanced Electrochemical Performance for Full Cell Lithium Ion Batteries*. Scientific reports, **7**, 44838 (2017).

6. Park, M.-H.; Kim, M. G.; Joo, J.; Kim, K.; Kim, J.; Ahn, S.; Cui, Y.; Cho, J., *Silicon Nanotube Battery Anodes.* Nano letters, **9**, 3844-3847 (2009).

7. Zhao, K.; Pharr, M.; Vlassak, J. J.; Suo, Z., *Inelastic hosts as electrodes for high-capacity lithium-ion batteries*. Journal of Applied Physics, **109**, 016110 (2011).

8. Zhao, K.; Wang, W. L.; Gregoire, J.; Pharr, M.; Suo, Z.; Vlassak, J. J.; Kaxiras, E., *Lithium-Assisted Plastic Deformation of Silicon Electrodes in Lithium-Ion Batteries: A First-Principles Theoretical Study*. Nano letters, **11**, 2962-2967 (2011).

9. Magasinski, A.; Dixon, P.; Hertzberg, B.; Kvit, A.; Ayala, J.; Yushin, G., *High-performance lithium-ion anodes using a hierarchical bottom-up approach.* Nature Materials, **9**, 353 (2010).

10. Chan, C. K.; Peng, H.; Liu, G. A. O.; McIlwrath, K.; Zhang, X. F.; Huggins, R. A.; Cui, Y. I., *High-performance lithium battery anodes using silicon nanowires.* In Materials for Sustainable Energy, Co-Published with Macmillan Publishers Ltd, UK; pp 187-191 (2010).

11. Liu, X. H.; Zhong, L.; Huang, S.; Mao, S. X.; Zhu, T.; Huang, J. Y., *Size-Dependent Fracture of Silicon Nanoparticles During Lithiation.* ACS Nano, **6**, 1522-1531 (2012).

12. Liu, C.; Li, C.; Ahmed, K.; Mutlu, Z.; Ozkan, C. S.; Ozkan, M., *Template Free and Binderless NiO Nanowire Foam for Li-ion Battery Anodes with Long Cycle Life and Ultrahigh Rate Capability*. Scientific reports, **6**, 29183 (2016).

13. Ko, M.; Chae, S.; Ma, J.; Kim, N.; Lee, H.-W.; Cui, Y.; Cho, J., *Scalable synthesis of silicon-nanolayer-embedded graphite for high-energy lithium-ion batteries.* Nature Energy**, 1**, 16113 (2016).

14. Hu, L.; Liu, N.; Eskilsson, M.; Zheng, G.; McDonough, J.; Wågberg, L.; Cui, Y., *Silicon-conductive nanopaper for Li-ion batteries.* Nano Energy, **2**, 138-145 (2013).

15. Lu, Z.; Liu, N.; Lee, H.-W.; Zhao, J.; Li, W.; Li, Y.; Cui, Y., *Nonfilling Carbon Coating of Porous Silicon Micrometer-Sized Particles for High-Performance Lithium Battery Anodes.* ACS Nano, **9**, 2540-2547 (2015).

16. McDowell, M. T.; Woo Lee, S.; Wang, C.; Cui, Y., *The effect of metallic coatings and crystallinity on the volume expansion of silicon during electrochemical lithiation/delithiation.* Nano Energy**, 1**, 401-410 (2012).

17. Yao, Y.; Liu, N.; McDowell, M. T.; Pasta, M.; Cui, Y., *Improving the cycling stability of silicon nanowire anodes with conducting polymer coatings*. Energy & Environmental Science, **5**, 7927-7930 (2012).

18. Wu, H.; Yu, G.; Pan, L.; Liu, N.; McDowell, M. T.; Bao, Z.; Cui, Y., *Stable Li-ion battery anodes by in-situ polymerization of conducting hydrogel to conformally coat silicon nanoparticles.* Nature communications, **4**, 1943 (2013).

19. Werner Stöber, A. F., *Controlled Growth of Monodisperse Silica Spheres in the Micro Size Range.* Journal of Colloid and Interface Science, **26**, 62-69 (1968).

20. Wang, W.; Favors, Z.; Ionescu, R.; Ye, R.; Bay, H. H.; Ozkan, M.; Ozkan, C. S., *Monodisperse porous silicon spheres as anode materials for lithium ion batteries*. Scientific reports, 5, 8781 (2015).

21. Xie, J.; Wang, G.; Huo, Y.; Zhang, S.; Cao, G.; Zhao, X., *Nanostructured silicon spheres prepared by a controllable magnesiothermic reduction as anode for lithium ion batteries*. Electrochimica Acta, **135**, 94-100 (2014).

22. Ng, L. V.; McCormick, A. V., Acidic Sol−Gel Polymerization of TEOS: *Effect of Solution Composition on Cyclization and Bimolecular Condensation Rates*. The Journal of Physical Chemistry, **100**, 12517-12531 (1996).

23. Bao, Z.; Weatherspoon, M. R.; Shian, S.; Cai, Y.; Graham, P. D.; Allan, S. M.; Ahmad, G.; Dickerson, M. B.; Church, B. C.; Kang, Z.; Abernathy, H. W., 3rd; Summers, C. J.; Liu, M.; Sandhage, K. H., *Chemical reduction of three-dimensional silica micro-assemblies into microporous silicon replicas*. Nature, **446**, 172-5 (2007).

24. Wang, W.; Ruiz, I.; Ahmed, K.; Bay, H. H.; George, A. S.; Wang, J.; Butler, J.; Ozkan, M.; Ozkan, C. S., *Silicon Decorated Cone Shaped Carbon Nanotube Clusters for Lithium Ion Battery Anodes*. Small, **10**, 3389-3396 (2014).

25. Favors, Z.; Wang, W.; Bay, H. H.; Mutlu, Z.; Ahmed, K.; Liu, C.; Ozkan, M.; Ozkan, C. S., *Scalable Synthesis of Nano-Silicon from Beach Sand for Long Cycle Life Li-ion Batteries.* Scientific reports, **4**, 5623 (2014).

26. Bell, J.; Ye, R.; Ahmed, K.; Liu, C.; Ozkan, M.; Ozkan, C. S., *Free-standing Ni–NiO nanofiber cloth anode for high capacity and high rate Li-ion batteries*. Nano Energy, **18**, 47-56 (2015).

27. Campbell, B.; Ionescu, R.; Tolchin, M.; Ahmed, K.; Favors, Z.; Bozhilov, K. N.; Ozkan, C. S.; Ozkan, M., *Carbon-Coated, Diatomite-Derived Nanosilicon as a High Rate Capable Li-ion Battery Anode.* Scientific reports, **6**, 33050 (2016).

Chapter 4: Facile and Scalable Synthesis of Copolymer-Sulfur Composites as Cathodes for High Performance Lithium-Sulfur Batteries

4.1 Instruction

Nowadays, energy storage is playing an essential role in the field of consumer electronics, electric vehicles, aerospace applications, and stationary energy storage[1, 2]. Lithium-ion batteries (LIBs) have been the key technology of the rechargeable batteries, considering their high energy-density, low operation voltage, and low rate of self-discharge. However, the capacity of LIBs is still limited. Many efforts have been focused on improving the capacities of LIBs, such as novel anode materials[3-7] and high capacity cathodes[8]. Sulfur is one of the promising cathode materials, because of its high specific capacity, which is 5 times more than that of LiCoO2. However, there are several challenges impeding its commercialization: a). volume expansion (80%) during charge/discharge process; b). low conductivity of Li2S (10-15 cm2 s-1)[9]; c). polysulfide shuttling. In particular, to suppress the polysulfide shuttling, it has been proposed to use carbon-sulfur composite cathode[10, 11], graphene encapsulation sulfur cathodes[12-14] and polymer coated sulfur cathodes[15, 16]. Apart from the stability, scalability of sulfur cathodes is required for commercialization as well. It has been reported that large scale synthesis of copolymer sulfur cathodes can be achieved by inverse vulcanization[17-19]. In detail, 1,3-diisopropenylbenzene (DIB) is applied to quench diradicals of sulfur chains and to obtain poly(sulfur-random-DIB). Moreover, 1,4-diphenylbutadiyne[20] and 1,4 dicyanobenzene[21] were also used to synthesize the copolymer-sulfur cathodes. Besides those chemicals, 1,3 diethynylbezene (DEB) has potential to be another precursor as

well[22] . However, there are still few report on this topic. In this article, we propose a method that applying DEB as the precursor and synthesizing the copolymer composite at lower temperature and under ambient.

4.2 Experiments

4.2.1 Material Synthesis

Firstly, the sulfur was heated to 120 ºC in silicon oil bath under an ambient atmosphere to melt the sulfur. Secondly, the clear yellow sulfur liquid was heated further till 140 ºC. After that, a certain amount of 1,3-diethynylbenzene (DEB), was added into the sulfur liquid (S:DEB=4:1, wt%). The mixture was heated and stirred at 140 ºC for five minutes. When the products were naturally cooled down to room temperature, we obtained the glass-like copolymer-sulfur composite materials. The composite was grounded into powders under an ambient atmosphere.

4.2.2 Material Characterization

We used the thermogravimetric analysis (TGA) and derivative thermogravimetric analysis (DTG) to determine the sulfur content and the evaporation temperature of the copolymer-sulfur composite under a nitrogen (N_2) atmosphere at a temperature range of 30 ºC to 600 ºC with a heating rate of 20 ºC/min.

X-ray photoelectron spectroscopy (XPS) were carried out using a Kratos AXIS ULTRADLD XPS system equipped with an Al Kα monochromated X-ray source. The size of slot for XPS is 300 μm x 700 μm. The vacuum pressure was kept below 3 x 10^{-9}

Torr, and the neutralizer was applied during the data acquisition. The XPS spectra were calibrated to the position of the C-C peak of 284.6 eV.

4.2.3 Electrochemical Performance

The half-cells were fabricated using the copolymer-sulfur cathodes, which were prepared by mixing 50% copolymer-sulfur composites, 40% acetylene black (AB) and 10% Poly(vinylidene fluoride) (PVDF) in the N-methyl-2-pyrrolidone (NMP) solvent.

The electrochemical performance of the copolymer-sulfur cathode was tested by various electrochemical measurements including cyclic voltammetry (CV), and galvanostatic charge/discharge.

4.3 Results and Discussion

The most stable format of elemental sulfur is the eight-membered ring (S_8) with melting point of 120 ºC ~ 125 ºC. When the sulfur is heated further to 160 ºC, which is named as the floor temperature, the sulfur ring is changed into linear polysulfane with radical ends. This phenomenon is called as ring opening polymerization (ROP)[17].

Fig.4. 1 Illustration to ROP of Elemental Sulfur

The precursor of liquid sulfur to stabilize polymerize the linear DEB is added to the the radical ends to sulfur as shown in Fig. 4.2. The as-produced

organo-sulfur composites are glass-like and dark yellow solid in Fig. 4.3.

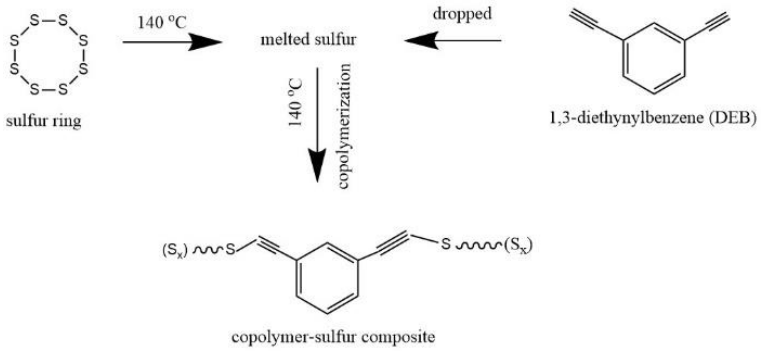

Fig.4. 2 Illustration of the synthesis process of the copolymer-sulfur composite

Fig.4. 3 As-produced Glass-Like Organo-sulfur Materials

The high sulfur content in the copolymer-sulfur composite was confirmed by TGA (figure 2a), which is ~86 wt.%. The DTG plot (figure 2b) reveals that the complete evaporation of sulfur from the copolymer-sulfur composite occurs at a temperature above the evaporation temperature of elemental sulfur. This suggests a higher energy binding interaction of carbon and sulfur in the copolymer-sulfur composite.

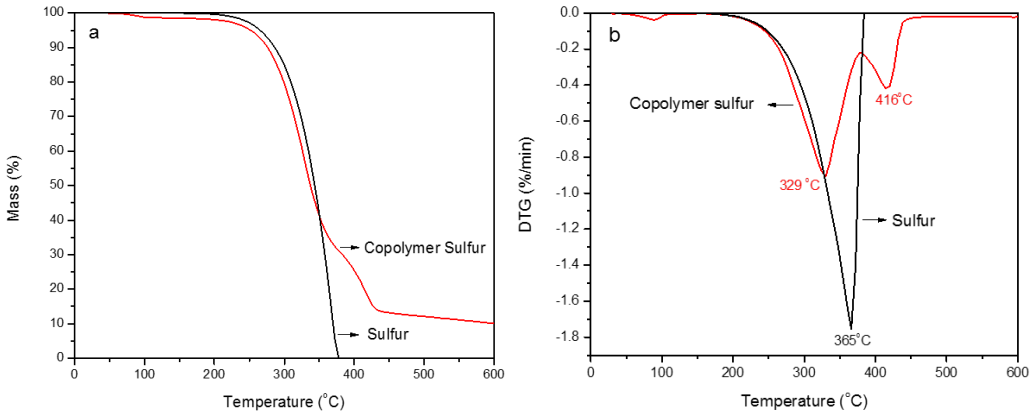

Fig.4. 4 TGA (a) and DTG (b) plots of the copolymer-sulfur composite

XPS analysis were performed confirm the presence of carbon and sulfur in the copolymer-sulfur composite, and to identify the nature of their chemical bonds. The high-resolution S 2p peak (figure 3a) was fitted to three peaks at binding energies of 163.7 eV, 164.8 eV, and 165.8 eV, respectively. Two major peaks located at 163.7 eV and 164.8 eV correspond to the S-S bonds in S_8[23]. The minor and broad peak at 165.8 eV is assigned to the C-S bonds[23]. The high-resolution C1s peak (figure 3b) was deconvoluted to two peaks at binding energies of 284.6 eV and 286.6 eV. The sharp and intense peak at 284.6

eV belongs to the C-C bonds[23]. The higher energy broader peak is attributed to the C-S bonds[23]. The high-resolution S 2p and C 1s peaks are well consistent with the literature values[24].

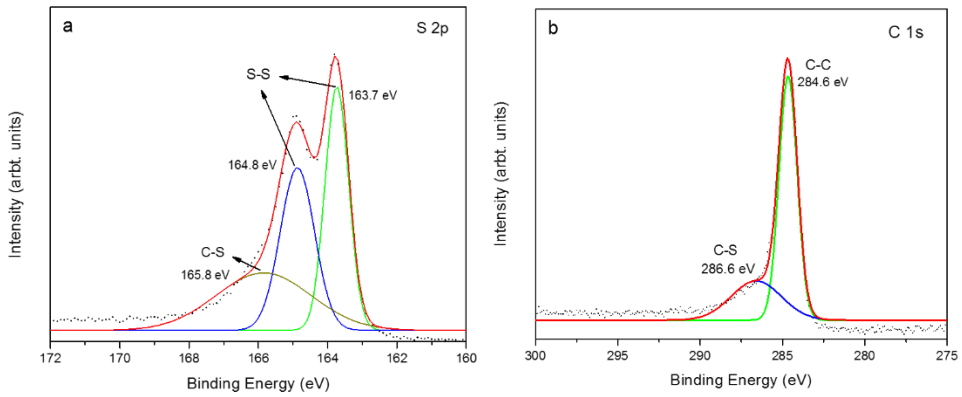

Fig.4. 5 Core level XPS spectra of (a) S 2p, and (b) C 1s of copolymer-sulfur composites

To examine the electrochemical performance of organo-sulfur cathode, we made a LIB with our sulfur cathode via a traditional hall-cell configuration. The SEM images of the sulfur cathode was shown in Fig. 4.7 (a), while the EDX mapping indicated the uniformly mixed conductivity additive and active materials of organo-sulfur.

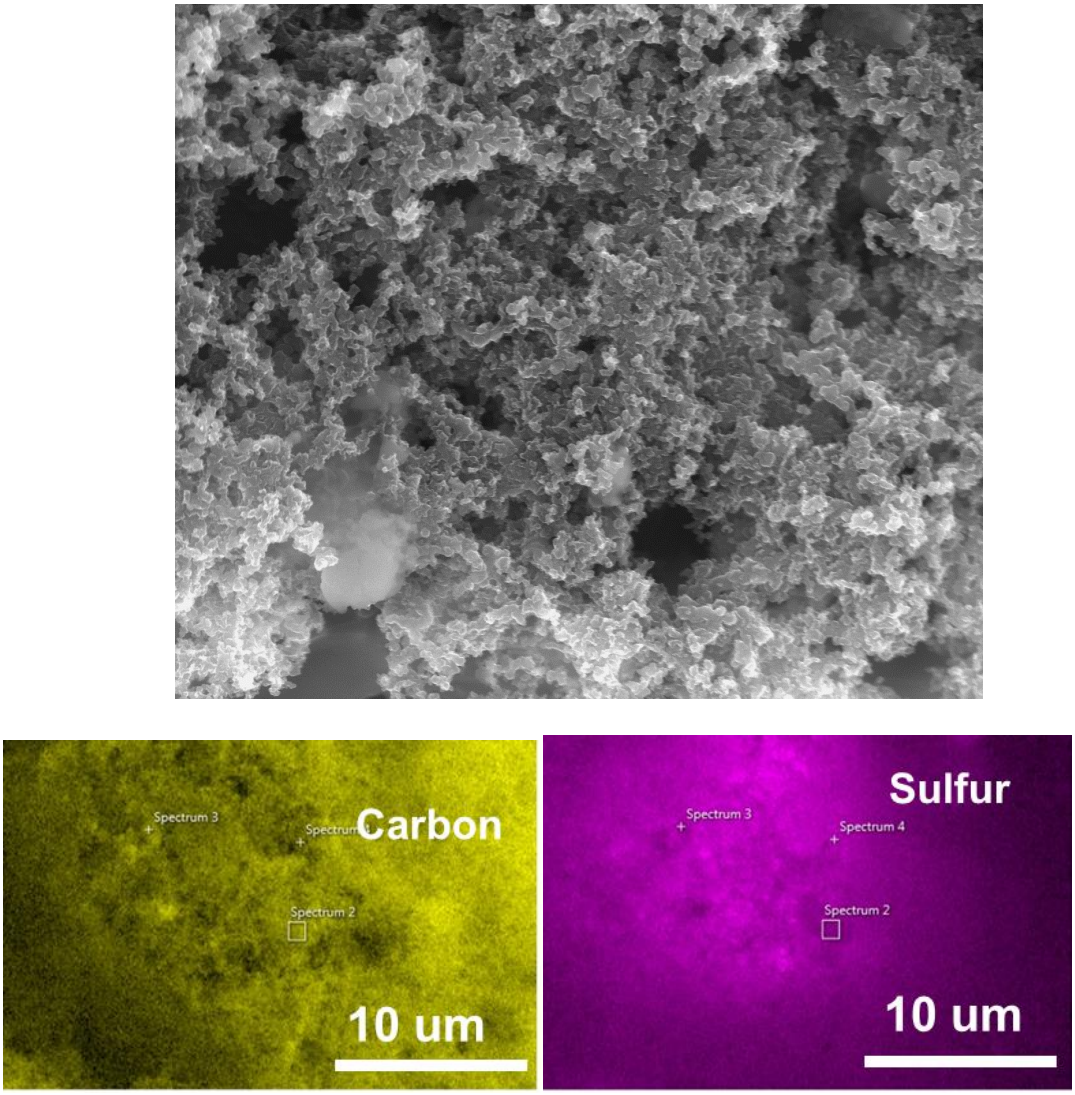

Fig.4. 6 (a)SEM Images, (b)&(c)EDX Mapping of As-prepared Sulfur Cathode

CV was conducted to study the electrochemical behavior of the copolymer-sulfur composite cathodes. In the CV plot (figure 4), two reduction peaks were observed at 2.05 V and 2.35 V, respectively. The organosulfur-DEB units and sulfur chains transformed into the higher-order polysulfide at 2.35 V and further reduced into the lower-order

polysulfide at 2.05 V. Two oxidation peaks were also observed at 2.33 V and 2.4 V, respectively. The lower-order polysulfide was oxidized to the higher-order polysulfide at 2.33 V. The further oxidation occured at 2.4 V, leading to oxidation of the higher-order polysulfide to element sulfur [25-26].

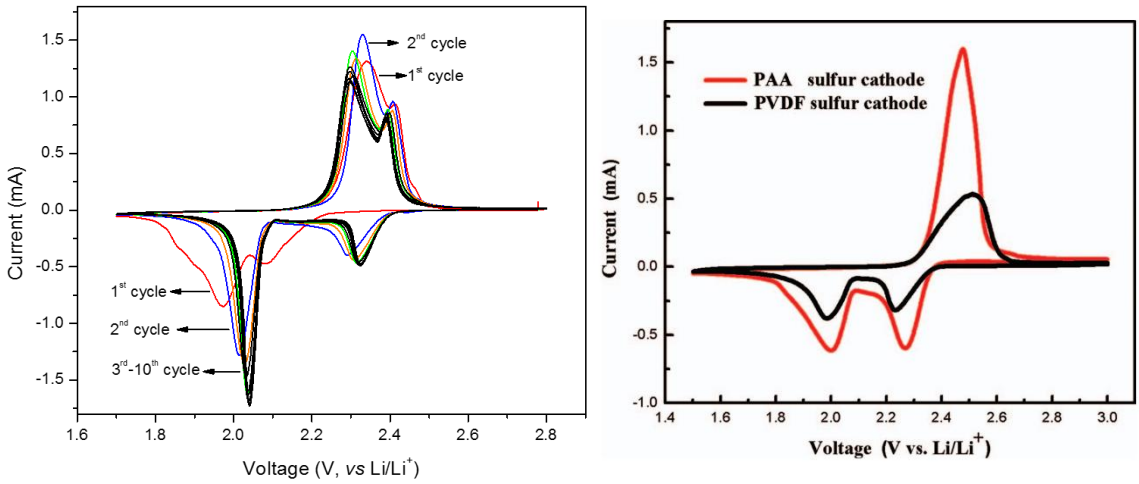

Fig.4. 7 CV of the (a)Organo-Sulfur Cathode (b) Traditional Elemental Sulfur Cathode

No significant changes were observed in the reduction/oxidization curves after 5th cycles, indicating that the charge/discharge performance of the copolymer-sulfur cathode was stabilized. The copolymer-sulfur cathode demonstrated a discharge capacity of 1042 mAh g^{-1} for the 1st cycle (figure 4.8 (a)). The capacity faded and demonstrated a capacity of 489 mAh g^{-1} over 300 cycles. The calculated capacity retention was ~ 47%. In addition, we did not observe any typical voltage plateau for the higher-order polysulfide formation for the 1st cycle, while it appeared at the 6th and 300th cycles (figure 4.8 (b)).

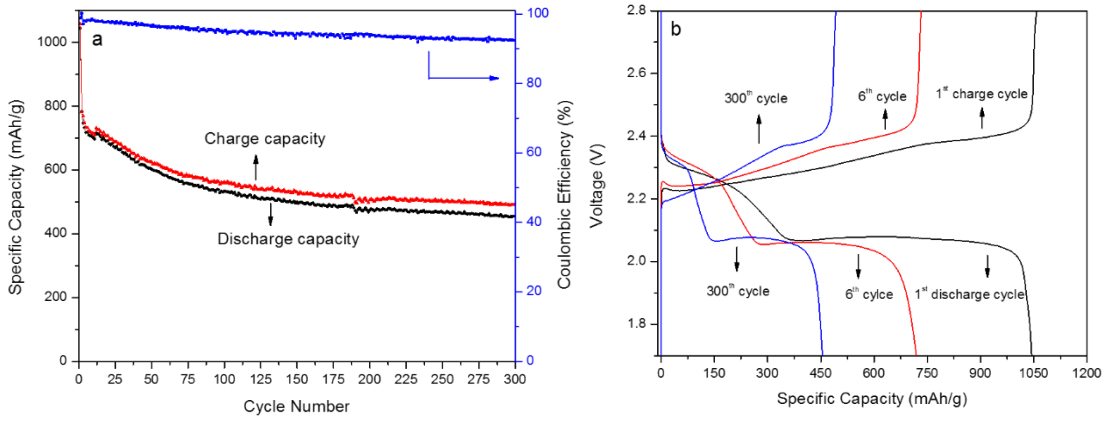

Fig.4. 8 charge/discharge capacities and coulombic efficiency over cycles

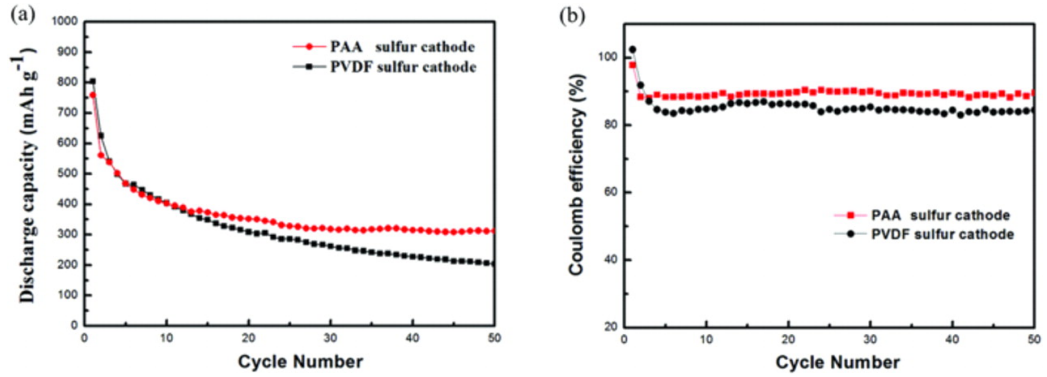

Fig.4. 9 Cycling Performance and Columbic Efficiency of Traditional Sulfur Cathodes

To better understand the origin of the capacity decrease over the cycles, we proposed an electrochemical (EC) reaction of the organosulfur-DEB units during the discharge/charge process (figure 6). When the copolymer-sulfur composite cathode is discharged at a high voltage (>2.1 V), the organosulfur-DEB units, and sulfur chains or

sulfur rings are reduced into the organosulfur-DEB-Li units and the high-order polysulfide[24b]. When the cell is discharged further, the organosulfur-DEB units are further reduced as well as the orders of the polysulfide. When the voltage is less than 2.1 V, the organosulfur-DEB units are fully discharged, where every unit is connected to a Li-ion, and the insoluble Li_2S forms onto the surface of the cathode. Therefore, we can conclude that the formation of the polysulfide is generally accompanied by the discharged organosulfur-DEB units. While the sulfur chains or sulfur rings mostly contribute to the capacity, the organosulfur-DEB units here mainly serve as the 'plasticizers' to prevent the dissolution of the high-order polysulfide[18]. We believe that the decrease in the capacity over the several cycles can be caused by the partial decomposition of the organosulfur-DEB units and concentrated organosulfur-DEB units[18]. It was further verified by the Raman shift before and after cycles. After 5 cycles, the peak representing C-S bonding was weakened and broadened shown in Fig. 4.11.

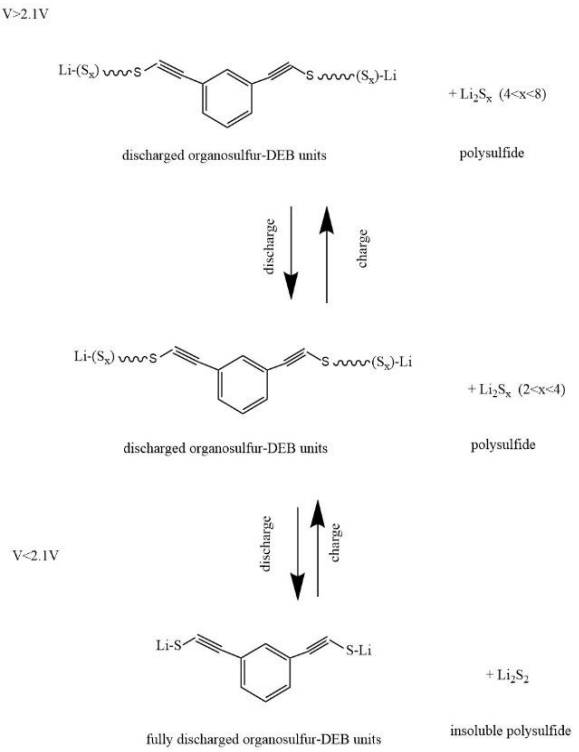

Fig.4. 10 Proposed EC reactions occurring during the discharge/charge process

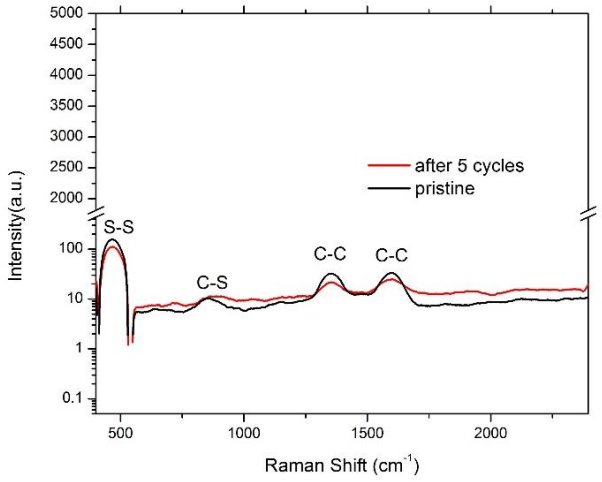

Fig.4. 11 Raman Shift Before and After Cycles

4.4 Conclusion

In conclusion, we have synthesized a copolymer-sulfur composite as a promising cathode material for lithium-sulfur batteries using sulfur and DEB via inverse vulcanization at lower temperature under ambient conditions. The battery utilizing the copolymer-sulfur cathode with high sulfur content demonstrates a relatively improved discharge/charge performance, with a capacity retention of ~ 47% after 300 cycles. The organosulfur-DEB units in the copolymer-sulfur composite cathode, acting as plasticizers, can effectively improve the stability of the battery, which is a distinct advantage over elemental sulfur cathodes. To further improve the stability of orgno-sulfur units, we can operate the synthesis process at a higher temperature, such as 200 ^{o}C. In consideration of the flammability of organic precursors, it is better to carry out the polymerization in glove box filled with Ar with controlled low O_2 and H_2O (<1.5 ppm).

4.5 Reference

1. W. Wang, Z. Favors, C. Li, C. Liu, R. Ye, C. Fu, K. Bozhilov, J. Guo, M. Ozkan and C. S. Ozkan, Sci.Rep. **7**, 44838 (2017).

2. C. Liu, C. Li, K. Ahmed, W. Wang, I. Lee, F. Zaera, C. S. Ozkan and M. Ozkan, RSC Adv. **6** (85), 81712-81718 (2016).

3. C. Li, C. Liu, W. Wang, J. Bell, Z. Mutlu, K. Ahmed, R. Ye, M. Ozkan and C. S. Ozkan, Chem.Commun. **52** (76), 11398-11401 (2016).

4. C. Li, C. Liu, W. Wang, Z. Mutlu, J. Bell, K. Ahmed, R. Ye, M. Ozkan and C. S. Ozkan, Sci.Rep. **7** (1), 917 (2017).

5. C. Liu, C. Li, W. Wang, M. Ozkan and C. S. Ozkan, Ener. Tech. **5** (3), 422-427 (2017).

6. C. Liu, C. Li, K. Ahmed, Z. Mutlu, C. S. Ozkan and M. Ozkan, Sci. Rep. **6**, 29183 (2016).

7. C. Liu, C. Li, K. Ahmed, W. Wang, I. Lee, F. Zaera, C. S. Ozkan and M. Ozkan, Adv. Mater. Interf. **3** (6), 1500503 (2016).

8. J. W. Fergus, J. Power Sources **195** (4), 939-954 (2010).

9. Y. Yang, G. Zheng and Y. Cui, Chem. Soc. Rev. **42** (7), 3018-3032 (2013).

10. C. Liang, N. J. Dudney and J. Y. Howe, Chem. Mater. **21** (19), 4724-4730 (2009).

11. G. Zheng, Q. Zhang, J. J. Cha, Y. Yang, W. Li, Z. W. Seh and Y. Cui, Nano Lett. **13** (3), 1265-1270 (2013).

12. S. Evers and L. F. Nazar, Chem. Commun. **48** (9), 1233-1235 (2012).

13. H. Wang, Y. Yang, Y. Liang, J. T. Robinson, Y. Li, A. Jackson, Y. Cui and H. Dai, Nano lett. **11** (7), 2644-2647 (2011).

14. J.-Z. Wang, L. Lu, M. Choucair, J. A. Stride, X. Xu and H.-K. Liu, J. Power Sources **196** (16), 7030-7034 (2011).

15. W. Li, G. Zheng, Y. Yang, Z. W. Seh, N. Liu and Y. Cui, Proc. Acad. Sci. U. S. A. **110** (18), 7148-7153 (2013).

16. W. Zhou, X. Xiao, M. Cai and L. Yang, Nano lett. **14** (9), 5250-5256 (2014).

17. W. J. Chung, J. J. Griebel, E. T. Kim, H. Yoon, A. G. Simmonds, H. J. Ji, P. T. Dirlam, R. S. Glass, J. J. Wie, N. A. Nguyen, B. W. Guralnick, J. Park, SomogyiÁrpád, P. Theato, M. E. Mackay, Y.-E. Sung, K. Char and J. Pyun, Nat. Chem. **5** (6), 518-524 (2013).

18. A. G. Simmonds, J. J. Griebel, J. Park, K. R. Kim, W. J. Chung, V. P. Oleshko, J. Kim, E. T. Kim, R. S. Glass, C. L. Soles, Y.-E. Sung, K. Char and J. Pyun, ACS Macro Lett. **3** (3), 229-232 (2014).

19. J. J. Griebel, G. Li, R. S. Glass, K. Char and J. Pyun, J. Polym. Sci. A Polym. Chem **53** (2), 173-177 (2015).

20. P. T. Dirlam, A. G. Simmonds, T. S. Kleine, N. A. Nguyen, L. E. Anderson, A. O. Klever, A. Florian, P. J. Costanzo, P. Theato, M. E. Mackay, R. S. Glass, K. Char and J. Pyun, RSC Adv. **5** (31), 24718-24722 (2015).

21. S. N. Talapaneni, T. H. Hwang, S. H. Je, O. Buyukcakir, J. W. Choi and A. Coskun, Angew. Chem **55** (9), 3106-3111 (2016).

22. Z. Sun, M. Xiao, S. Wang, D. Han, S. Song, G. Chen and Y. Meng, J. Mater. Chem. A **2** (24), 9280 (2014).

23. https://srdata.nist.gov/xps/Default.aspx.

24. G. Zhou, in *Design, Fabrication and Electrochemical Performance of Nanostructured Carbon Based Materials for High-Energy Lithium–Sulfur Batteries: Next-Generation High Performance Lithium–Sulfur Batteries* (Springer Singapore, Singapore, 2017), pp. 57-74.

25. Y. Fu and A. Manthiram, RSC Adv. **2** (14), 5927 (2012).

26. Y. Li, Z. Li, Q. Zhang and P. K. Shen, J. Mater. Chem. A **2** (13), 4528 (2014).